UNIVERSITY OF OKLAHOMA

GRADUATE COLLEGE

MULTISCALE SIMULATIONS OF HEAT TRANSFER IN NANOCOMPOSITES

A DISSERTATION

SUBMITTED TO THE GRADUATE FACULTY

in partial fulfillment of the requirements for the

Degree of

DOCTOR OF PHILOSOPHY

By

KHOA NGUYEN DANG BUI
Norman, Oklahoma
2012

MULTISCALE SIMULATIONS OF HEAT TRANSFER IN NANOCOMPOSITES

A DISSERTATION APPROVED FOR THE
SCHOOL OF CHEMICAL, BIOLOGICAL AND MATERIALS ENGINEERING

BY

_____
Dr. Dimitrios V. Papavassiliou, Chair

_____
Dr. Daniel E. Resasco

_____
Dr. Alberto Striolo

_____
Dr. I. Yucel Akkutlu

_____
Dr. Takumi Hawa

I would like to dedicate this dissertation to my parents. They are always by my side with tremendous love and support in the pursuit of my education.

Acknowledgements

Table of Contents

List of Tables

List of Figures

Abstract

The field of nanotechnology has been expanded by the discovery of fullerenes and carbon nanotubes (CNTs) in the 20th century. Geim and Novoselov won the Nobel prize in 2010 for their work on graphene sheets (GSs). Those materials with their outstanding properties have been suggested as reinforcement fillers in a variety of composite materials. By incorporating these nanomaterials into a polymer matrix, or dispersing them into a solution, the effective thermal conductivity of the resulting composite (K_{eff}) can be increased. For example, this enhancement can range from 80% to 125% at 1.0wt% of CNTs over pure polymer for the case of epoxy composites or by a factor of almost 4 in the case of high concentration of single-walled carbon nanotubes (SWNTs) in poly-styrene. However, based on the properties of pristine CNTs and GSs, one would expect a much higher value of K_{eff} of such composites, more than one order of magnitude according to the classical theory of Maxwell. The presence of resistance to heat transfer at the nanoinclusion-polymer interface, known as the interfacial thermal resistance or Kapitza resistance, is the reason for this difference.

Experimentally measuring and characterizing heat transport at the nanoscale are not trivial tasks and current theory in this area is limited to simple cases only. The acoustic mismatch theory and the effective medium theory provide a rough estimation of Kapitza resistance and K_{eff} of the composites, respectively. However, the effect of dispersion pattern and the orientation of nanoinclusions inside the polymer matrix on K_{eff} is still an open question. For the case of multi-walled carbon nanotubes (MWCNTs) embedded in polymer matrix, it is unknown whether thermal transfer occurs solely via the outermost wall or through the center of the tube.

In this work, Monte Carlo (MC) simulations were developed to investigate heat transfer in nanocomposites. This approach is capable of taking into account the effect of different geometries, realistic orientations, and dispersion patterns of nanoinclusions on K_{eff}. Furthermore, molecular dynamics (MD) simulations were employed coherently with MC simulations to characterize interfacial thermal resistance. Results from this work provide suggestions for producing superior thermal nanocomposites through the controll of Kapitza resistance and the configurations of nanoinclusions inside the polymer matrix.

Chapter 1: Introduction

1.1.   Thermal properties of carbon nanotubes and graphene sheets

Heat dissipation continues to be a major challenge in the modern electronics industry as a result of miniaturization efforts.[1] The need for superior heat-conducting materials became essential for design of the next generations of integrated circuits.[2] Similar thermal needs have been encountered in optoelectronics and photonics devices.[3] On the other hand, thermal insulator materials, which have the ability to strongly suppress thermal conductivity, are required to conserve energy in aerospace and other applications.

Thermal conductivity (K) is a material property defined as the ability to conduct heat. It is introduced in Fourier's Law for heat conduction in solid materials:

$$\vec{q} = -K\nabla T \tag{1.1.1}$$

where $\vec{q}$, K, ∇T are the local heat flux through a unit area per unit of time (Wm^{-2}), the thermal conductivity ($Wm^{-1}K^{-1}$), and temperature gradient (Km^{-1}), respectively. In anisotropic materials, K varies with orientation and is described by a tensor.

There are both electrons and atomic vibration in crystals, known as phonons, that contribute to heat conduction. Because there is high concentration of free carriers in metals, the mechanism of heat conduction in metals is dominated by electrons. The electron's contribution to thermal conductivity (K_e) can be determined from the electrical conductivity (σ) through the Wiedemann-Franz law:[4]

$$K_e = \sigma L_0 T \tag{1.1.2}$$

where the Lorenz number, L_0, equals 2.45×10^{-8} (V/K)^2 and T is the temperature in Kelvin. On the other hand, heat conduction in carbon-based materials is usually dominated by phonons even for graphite, which has metal-like properties.[5] The phonon thermal conductivity, K_p, is expressed as [6]

$$K_p = \sum_j \int C_j(\omega) v_j^2(\omega) \tau_j(\omega) d\omega \tag{1.1.3}$$

where j is the phonon branch, v_j is the phonon group velocity, τ_j is the phonon relaxation time and C_j is the heat capacity of the given branch j. The phonon mean free path λ, which is the average distance a phonon can move between two collisions or scattering events, is related to the relaxation time and phonon group velocity as

$$\lambda = \tau v \tag{1.1.4}$$

In solids, it is the acoustic phonons not the optical phonons that are responsible for carrying the bulk of heat. These phonons are usually scattered by other phonons, lattice defects, impurities, conduction electrons and interfaces that limit the value of K_p.[7] Based on the kinetic theory of ideal gases, K_p can also be calculated as [3, 8]

$$K_p = (1/3) C v \lambda = (1/3) C v^2 \tau \tag{1.1.5}$$

In nature, diamond possesses the highest thermal conductivity of any known bulk material. Due to very strong sp^3 carbon-to-carbon bond and light atomic mass, diamond crystals produce extremely high phonon frequencies and acoustic velocities.[9] Carbon nanotubes (CNTs) and Graphene Sheets (GSs) are allotropes of carbon that are 1-atom thick. This class of nanomaterials is composed entirely of sp^2 bonds, similar to those of graphite. These bonds, which are even stronger than sp^3 bonds found in diamond, provide CNTs and GSs with unique properties. The thermal conductivity of

CNTs and GSs has been experimentally measured or calculated to be higher than that of

diamond (Figure 1.1.1).
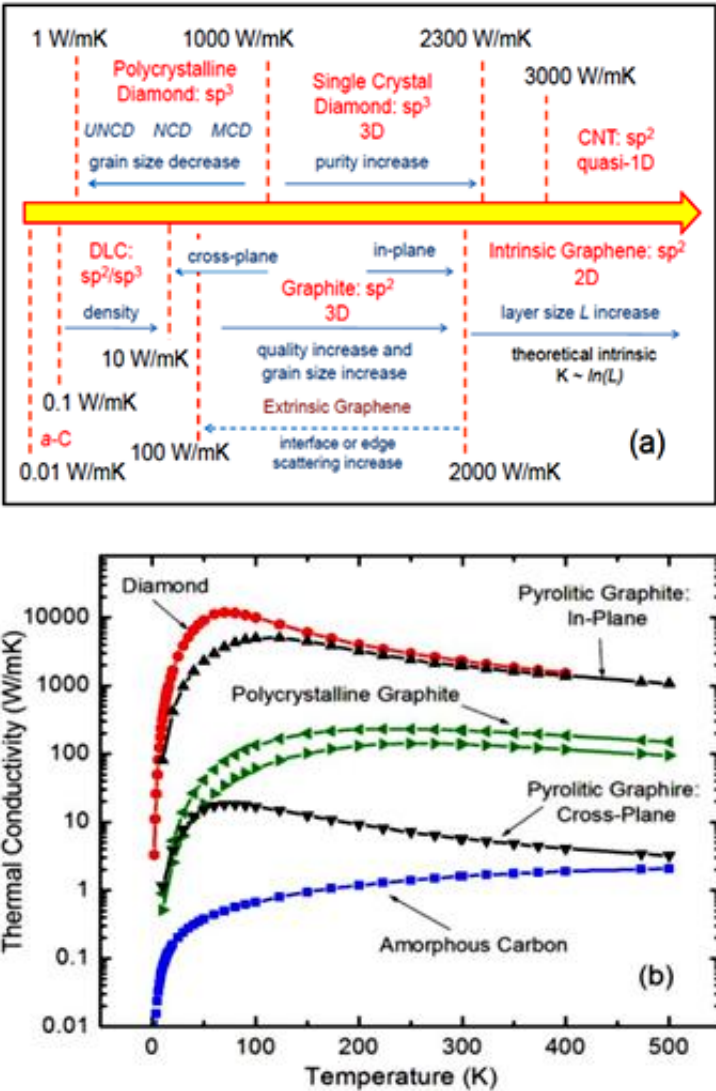
Figure 1.1.1. Thermal properties of carbon-based materials. (a) Average values of thermal conductivity. (b) Thermal conductivity of bulk carbon allotropes as a function of temperature. Reported by Balandin *et al.*[3]

Unlike bulk materials in which the phonon transport occurs in diffusive regimes,

heat conduction in CNTs and GSs happens in diffusive-ballistic regime. This is because

the phonon mean free path in these materials can exceed 500nm, even larger than the

length of the nanoinclusions.[10-12] As a result, K keeps increasing as the size of the

system increases (Figure 1.1.2). Benedict *et al*.[13] and Hone *et al*.[4] studied the specific heat of SWNTs and GSs over a wide range of temperatures. The ratio between the of phonon and electron contribution to the specific heat for these materials was reported to be 10^2-10^4.
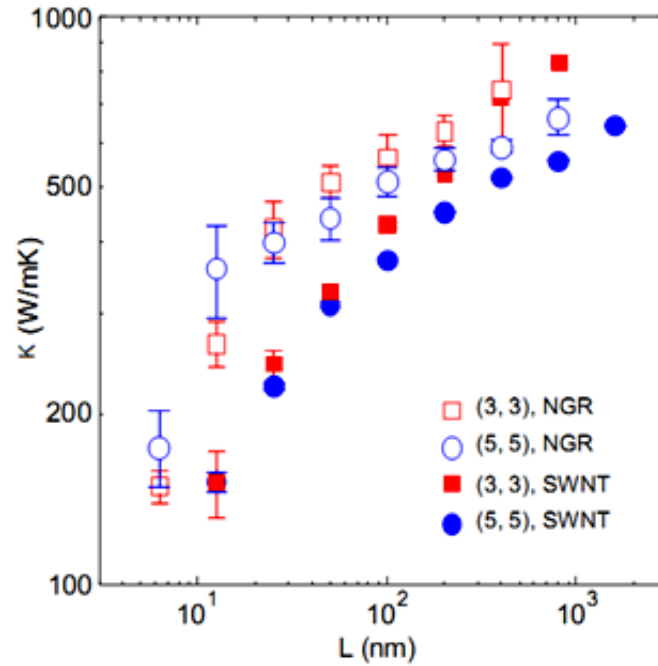
Figure 1.1.2. Length dependences of thermal conductivity (*K*) of single-walled carbon nanotubes (SWNT) and graphene nanoribbons (NGR) as calculated by Shiomi *et al*. Figure adapted from [14].

1.2. Interfacial thermal resistance

Interfacial thermal resistance, also known as thermal boundary resistance (TBR) or Kapitza resistance, is the resistance to thermal flow at the interface of two different materials (Figure 1.2.1). It was discovered in 1941 by Kapitza [15] at the interface of liquid helium and copper.

4
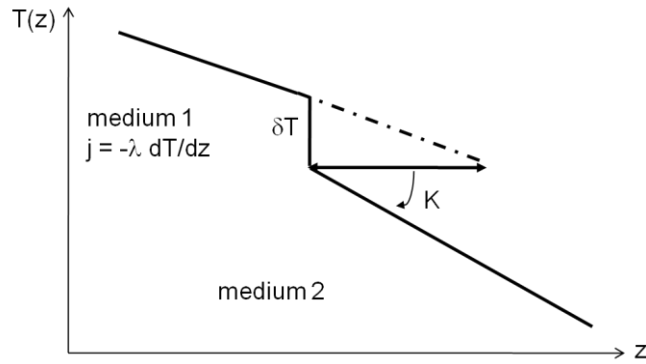
Figure 1.2.1. Plot of temperature distribution along the heat flux (z-direction) between two different mediums. There is a temperature drop and discontinuity (δT) at the interface due to Kapitza resistance.

The mechanism of this resistance remained unknown until Khalanikov *et al.*[16] proposed the acoustic mismatch model (AMM) in 1952. In this model, the heat flux is carried through the interface by acoustic waves propagating by the same law as the transmission of sound from one medium to another (Figure 1.2.2). Khalatnilov's model provides a possible explanation of the principle cause of Kapitza resistance. However, for some cases, predictions are almost one order of magnitude higher than experimental values.[17] Conserving the main idea that a major part of the heat flux through the interface is carried by acoustic waves, the diffuse mismatch model (DMM) developed by Swartz *et al.*[6] gives another estimation of Kapitza resistance.
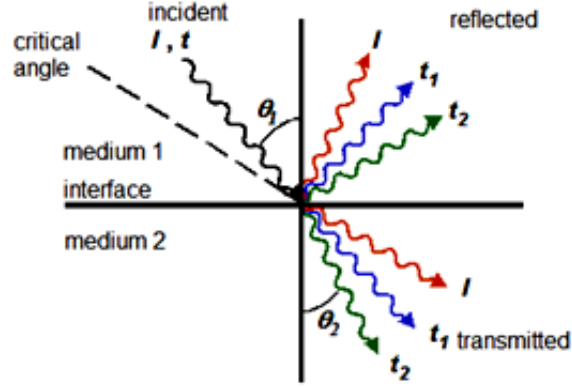
Figure 1.2.2. Schematic plot of the acoustic mismatch model developed by Khalatnikov *et al.* The incident phonons with 3 branches ,1 longitudinal and 2 transverse waves, will be reflected or transmitted at the interface of 2 different mediums. Figure adapted from ref. [16]

The phonon transmission probability, according to AMM model, is calculated as a function of incident phonons and properties at the interface as[18]

$$f_{1 \to 2} = \frac{4\rho_1 v_1 \cos\theta_2 \rho_2 v_2 \cos\theta_1}{(\rho_1 v_1 \cos\theta_2 + \rho_2 v_2 \cos\theta_1)^2} \tag{1.2.1}$$

where ρ_i, v_i, θ_i (the subscript i=1 or 2) are the density, sound velocity, angle between the phonon wave vector of medium i and the normal direction to the interface, respectively (Figure 1.2.2). The average phonon transmission probability, $f_{\text{avg}1 \to 2}$, is calculated as

$$f_{avg1 \to 2} = \int_0^{\pi/2} f_{1 \to 2}(\theta) \cos\theta \sin\theta d\theta \tag{1.2.2}$$

Thus, the Kapitza resistance, R_{bd}, can be approximated as[6]

$$R_{bd} = \frac{4}{\rho_1 v_1 C_1 f_{avg1 \to 2}} \tag{1.2.3}$$

where C_1 is the specific heat capacity of medium 1, other parameters are described as in Equation (1.2.1) and (1.2.2). A crucial assumption in the AMM model is that no scattering occurs at the interface. There were, however, experimental evidences that

high frequency phonons got scattered at the interface and opened up new channels for heat transport.[19] Hence, this assumption was replaced with the opposite extreme in the DMM model: all phonons are assumed to be diffusely scattered at the interface.[6] Because R_{bd} is inversely proportional to $f_{avg1\rightarrow2}$, the DMM model usually predicts Kapitza resistance as much as two orders of magnitude lower than experimental observations [20]. There have been lots of work to improve the acoustic models for better estimation of Kapitza resistance.[20-26]

It is also essential to point out what will happen if both sides of the interface are identical. In that case, the value of $f_{1\rightarrow2}$ and $f_{avg1\rightarrow2}$ are unity and 0.5, respectively. According to Equation (1.2.3), the Kapitza resistance does not vanish but still exists. Note that, this thermal resistance differs from contact resistance, as it exists even at atomically perfect interfaces. In general, this resistance is present at the interface between any materials and its value varies differently for each system.[27] Based on acoustic theory, [6] the more differences in density and sound velocity of two materials, the greater the value of Kapitza resistance will be. This is why the Debye temperature, the temperature at which the maximum frequency of phonon is activated, is often used to qualitatively compare the Kapitza resistance. For example, at room temperature, R_{bd} of Bi/diamond was measured to be $11.7 \times 10^{-8} W^{-1} m^2 K$ [28, 29], which is among the highest resistances for bulk materials. Bismuth is a metal containing free electrons as primary heat carriers, while diamond is a good insulator. As a result, the energy transport by means of electrons between these materials is suppressed. Furthermore, bismuth, which has low Debye temperature, has many phonons at low frequencies. Diamond, on the other hand, has very high Debye temperature with high-frequency

phonons. The significant difference in Debye temperature means that phonons do not efficiently couple across the Bi/diamond interface. In nanocomposites, the Debye temperature of common polymers is about 400K or lower, while it is higher than 2000K for CNTs and GSs. That also explains why the Kapitza resistance is a bottleneck for the heat transfer in nanocomposites.

1.3. Effective thermal conductivity of nanocomposites

Composite materials consist of two or more materials combined in such a way that each constituent remains distinguishable. Most composites have two constituents: a matrix and a reinforcement. The reinforcement is usually much stronger and stiffer than the matrix, and gives the composite its improved properties. For the case of nanocomposites, the reinforcements, also called inclusions, are CNTs or GSs that are dispersed inside common polymers. In terms of thermal conductivity, each constituent has its own value of K and the composite can be treated as a homogeneous material with an effective thermal conductivity, K_{eff}.

1.3.1. Maxwell model

Estimation of the conductivity of heterogeneous solids was first contributed by Maxwell.[30] Considering a material made of spheres of thermal conductivity K_p embedded in a continuous matrix with thermal conductivity K_m. Maxwell showed that for small volume fraction ϕ, the effective thermal conductivity is

$$\frac{K_{eff}}{K_m} = 1 + \frac{3\phi}{\dfrac{K_p + 2K_m}{K_p - K_m} - \phi} \tag{1.3.1}$$

For non-spherical inclusions, the composite is anisotropic and K becomes a tensor. When square arrays of long cylinders are parallel to the z-axis (i.e. the direction of the heat flow), Rayleigh[31] showed that the zz component of the thermal conductivity tensor is

$$\frac{K_{eff,zz}}{K_m} = 1 + \frac{(K_p - K_m)\phi}{K_m} \quad (1.3.2)$$

and the other two components are

$$\frac{K_{eff,xx}}{K_m} = \frac{K_{eff,yy}}{K_m} = 1 + \frac{2\phi}{\dfrac{K_p + K_m}{K_p - K_m} - \phi + \dfrac{K_p - K_m}{K_p + K_m}(0.30584\phi^4 + 0.013363\phi^8 + ...)} \quad (1.3.3)$$

For complex nonspherical inclusions, no exact treatment is possible. Intended for simple unconsolidated granular beds, the following expression has proven successful:[8]

$$\frac{K_{eff}}{K_m} = \frac{(1-\phi) + \eta\phi(K_p / K_m)}{(1-\phi) + \eta\phi} \quad (1.3.4)$$

in which

$$\eta = \frac{1}{3}\sum_{k=1}^{3}\left[1 + (\frac{K_p}{K_m} - 1)g_k\right]^{-1} \quad (1.3.5)$$

The g_k is the shape factor for the granules of the medium, where $g_1 + g_2 + g_3 = 1$ must be satisfied. For spheres, $g_1 = g_2 = g_3 = 1/3$, and Equation (1.3.3) reduces to Equation (1.3.1). For unconsolidated solids, $g_1 = g_2 = 1/8$ and $g_3 = 3/4$.

1.3.2. Effective medium approximation

Since Maxwell's and Rayleigh's models originally could not take into account the Kapitza resistance, Hasselman and Johnson[32] extended these theories and derived

an effective medium approximation (EMA) for calculating K_{eff} that includes interfacial effects and particle size for simple inclusions. Nan *et al.* [33, 34] generalized the EMA for various particle geometries and orientations. Considering an ellipsoidal particle in the matrix, let θ be the angle between the material axis (z-direction) and the local particle symmetric axis. The orientation of this inclusion is calculated as

$$\langle \cos^2 \theta \rangle = \frac{\int \rho(\theta) \cos^2 \theta \sin \theta d\theta}{\int \rho(\theta) \sin \theta d\theta} \tag{1.3.6}$$

where $\rho(\theta)$ is a distribution function describing ellipsoidal particle orientation. The geometrical shape factor L_{ii} is given by

$$L_{11} = L_{22} = \begin{cases} \dfrac{p^2}{2(p^2-1)} - \dfrac{p}{2(p^2-1)^{3/2}} \cosh^{-1} p, & p > 1 \\[4mm] \dfrac{p^2}{2(p^2-1)} - \dfrac{p}{2(1-p^2)^{3/2}} \cosh^{-1} p, & p < 1 \end{cases} \tag{1.3.7}$$

$$L_{33} = 1 - 2L_{11} \tag{1.3.8}$$

where $p = a_3/a_1$ is the aspect ratio of the ellipsoid. The equivalent thermal conductivity along the symmetric axis of this ellipsoidal inclusion is calculated as[33]

$$K_{ii}^c = K_p /(1 + \gamma L_{ii} K_p / K_m) \tag{1.3.9}$$

with $\quad \gamma = \begin{cases} (2 + 1/p)\alpha, & p \geq 1 \\ (1 + 2/p)\alpha, & p \leq 1 \end{cases}$

and K_p, K_m are the thermal conductivity of the particle and the matrix, respectively. Here a dimensionless parameter α is defined by

$$\alpha = \begin{cases} a_k/a_1, & p \geq 1 \\ a_k/a_3, & p \leq 1 \end{cases} \tag{1.3.10}$$

in which a_k is the Kapitza radius, $a_k = R_{bd} K_m$. Generally, $0 \leq a_k < \infty$, with $a_k = 0$ corresponding to the perfect interface. For the case of completely randomly oriented

ellipsoidal inclusions, $<\cos^2\theta> = 1/3$ and the effective thermal conductivity of the isotropic composites becomes

$$K_{eff} = K_m \frac{3 + f[2\beta_{11}(1-L_{11}) + \beta_{33}(1-L_{33})]}{3 - f[2\beta_{11}L_{11} + \beta_{33}L_{33}]} \qquad (1.3.11)$$

where

$$\beta_{ii} = \frac{K_{ii}^c - K_m}{K_m + L_{ii}(K_{ii}^c - K_m)} \qquad (1.3.12)$$

1.3.3. Numerical approach

Heat transfer in nanocomposites has been simulated numerically with conventional numerical methods. [35, 36] A solution of the steady state heat conduction equation with finite element methods (FEM) taking into account the Kapitza resistance was first performed by Davis *et al.*[37] Considering a spherical inclusion of radius r embedded inside a matrix (Figure 1.3.1), the steady state heat conduction equation is

$$-\nabla \cdot (K\nabla T) = 0 \qquad (1.3.13)$$

where T is the temperature. In the matrix region, $K = K_m$ and in the particle $K = K_p$. At the interface, there is a temperature discontinuity given by $Q = \nabla T / R_{bd}$ and the heat flux Q is conserved across the interface (Figure 1.3.1). The value of K_{eff} of the composite is then found by integrating the flux over the surface as[37]

$$K_{eff} = \frac{1}{\pi L^2(-T_0/L)} \int_0^L 2\pi r dr(-K_m dT/dz) \qquad (1.3.14)$$
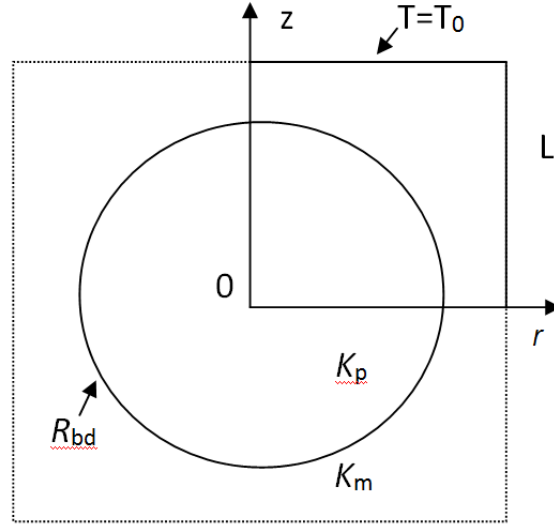
Figure 1.3.1. Axisymmetric model for computing the effective thermal conductivity of a composite of a matrix with thermal conductivity K_m and a spherical inclusion with thermal conductivity K_p. At the interface, there exists a Kapitza resistance R_{bd}.[37]

Results from this approach for spherical inclusions were in good agreement with experimental data and EMA[37]. Kumar *et al.* employed a similar approach to estimate K_{eff} of CNT-based nanocomposites.[35, 36] Based on the Fourier conduction equation in the CNTs and the substrate, the temperature distribution was calculated by a finite volume discretization scheme (FVD) and K_{eff} was calculated as

$$K_{eff} = \frac{\sum_{tubes} K_t A \frac{dT_i}{ds}\Big|_{x=0} + \sum_{subtrates} K_s \Delta y \Delta z \frac{dT_s}{ds}\Big|_{x=0}}{Ht\left(\frac{T_{drain} - T_{source)}}{L_C}\right)} \qquad (1.3.15)$$

This formula was derived by assuming CNTs as straight cylinder in thin box (2D). The first term in the numerator is the heat flow through the tubes in the lateral direction, while the second term represents the heat flow in the substrate. T_i and T_s are the temperature of tube segment and of the substrate, respectively. The computational

domain is represented by height (H), width (L_c) and thickness (t). K_t and K_s are the thermal conductivity of CNTs and substrate, respectively.

Note that Fourier's law of heat conduction assumes diffusive transport, while heat transfer in nanocomposites takes place in diffusive-ballistic regime due to the nano-sized inclusions.[3, 14, 38] Furthermore, measuring the electrical conductivity of CNT-based nanocomposites usually reveals a significant jump due to interconnecting network of tubes at very low wt.% of CNTs ($0.05 \div 4.0$ wt.% [39, 40]), while there is no analogous observation for the case of thermal conductivity.[41] Kumar *et al.*'s approach did not capture this behavior because values of Kapitza resistance at the interface of CNT-substrate and CNT-CNT were roughly assumed. These values can be measured by experiments, which is not a trivial task, or calculated by atomistic simulations.

1.4. Conclusions

In summary, K_{eff} of nanocomposites is a macroscopic property that depends on properties of the bulk material (density, sound velocity), the configuration of nanoinclusions (orientation, dispersion) and the atomistic property at the interface (Kapitza resistance). Unfortunately, most of the current models do not take into account all of the above effects due to the assumptions/simplifications made during the calculation of K_{eff}. The best approach to characterize Kapitza resistance at the interface is through atomistic simulations. However, due to computational cost, it is not efficient to employ this approach to calculate K_{eff} of nanocomposites when the number of nanoinclusions and polymer molecules are hundreds of thousands. Therefore, another class of simulations is required at the mesoscopic scale that can receive input from

atomistic simulations (Kaptiza resistance) and can explicitly consider the effect of realistic geometries and dispersion pattern of nanoinclusions on the calculation of K_{eff}. Details of this approach, based on off-lattice Monte Carlo simulations, are described in Chapter 2 – Methodology.

The main purpose of this work is not only to replicate the experimental results but also to quantitatively provide suggestions to improve K_{eff} of nanocomposites. In Chapter 3, we study the possibility of using another type of nanoinclusions with smaller Kapitza resistance than CNTs to enhance heat transfer. The importance of bundle-geometry on K_{eff} and a new type of Kapitza resistance at high vol.% of CNTs are discussed in Chapter 4. The question of whether the thermal energy transfer along a DWCNT occurs only through the outer CNT, or whether both CNTs contribute to heat transfer is answered in Chapter 5. Following that, K_{eff} of MWNT-based composites, taking into account all of the factors discussed above, and suggestions for improving K_{eff} are done in Chapter 6.

Chapter 2: Methodology

2.1. Molecular dynamic simulations

Molecular dynamics (MD) are very popular for simulating molecular-scale models of matter. This method was first developed in the 1950s, but it only began to attract widespread interest in the mid-1970s, when computers became powerful and affordable.[42] The essence of molecular dynamics can be simply stated as numerically solving the N-body problem of the classical equations of motion

$$m_i \ddot{\vec{r_i}} = \vec{f_i} \text{ and } \vec{f_i} = -\frac{\partial U}{\partial \vec{r_i}} \tag{2.1.1}$$

where m_i is the mass of atom i. For this purpose, one need to be able to calculate the forces $\vec{f_i}$ acting on the atoms, and these are usually derived from potential energy function $U(\vec{r}_N)$, where $\vec{r}_N = (r_1, r_2, \ldots, r_N)$ represents the complete set of 3N atomic coordinates.

In this work, MD simulations are performed with LAMMPS, Large−scale Atomic/Molecular Massively Parallel Simulator, which is an open source software developed at Sandia National Laboratories.[43]

2.1.1. Pair potentials and many-body potentials

The potential function, which is also called force field, is a function describing the interactions between particles in the simulation. The potential functions representing the non-bonded energy are calculated as a sum over interactions between the pair of particles in the system. The most popular of such a pair potential is the (12-6) Lennard-Jones (LJ) potential used for computing Van de Waals forces

$$U(r_d) = 4\varepsilon \left[\left(\frac{\sigma_{LJ}}{r_d} \right)^{12} - \left(\frac{\sigma_{LJ}}{r_d} \right)^{6} \right]$$

<div align="right">(2.1.2)</div>

where ε is the depth of the potential well, σ_{LJ} is the distance at which the inter-particle potential is zero and r_d is the distance between particles. For the case of many-body potentials, the potential energy cannot be found by a sum over pairs of atoms, as these interactions are calculated explicitly as a combination of higher-order terms. One example of such many-body potentials is the Tersoff potential,[44] which was originally used to simulate carbon, silicon and germanium, and has been used for a wide range of other materials. This potential involves a sum over groups of three atoms, with the angles between the atoms being an important parameter in the potential energy function.

By employing the appropriate potentials, MD simulations can be used to study a wide range of phenomena in science. For example, the REBO/AIREBO potential [44-46] can be used to simulate processes where chemical reactions occur. This is because, unlike molecular mechanics methods, the REBO/AIREBO force fields allow for bond-breaking and bond-formation to occur during the simulations.[47]

2.1.2. Non-equilibrium simulations

Non-equilibrium molecular dynamics (NEMD) simulations are employed in this work to quantify the Kapitza resistance at the interface of the system of interest. During the NVE ensemble, in which the system is isolated from changes in moles (N), volume (V) and energy (E), heat flow will take place across the interface from the hot side to the cold one. The temperature difference between two sides, ΔT, is recorded as a function of time, t, as

$$\Delta T(t) = \Delta T(t = 0)e^{-t/\tau}$$

<div align="right">(2.1.3)</div>

to obtain the time relaxation constant τ. The Kapitza resistance, R_{bd}, is calculated from the time constant via the following relation, based on the lump capacitance model:[48-51]

$$R_{bd} = \frac{A_T \tau}{C_T} \qquad (2.1.4)$$

where A_T is the interfacial area available for heat transfer.[52] The heat capacity of the hot side, C_T, is calculated via independent simulations as[49]

$$C_T = \frac{\langle E^2 \rangle - \langle E \rangle^2}{k_b T^2} \qquad (2.1.5)$$

where E is the total energy, k_b is the Boltzmann constant and T is the absolute temperature of the system. Note that this approach is formulated based on the lump capacitance model, which requires the Biot number, Bi, to be less than 0.1.[51, 53] The Biot number is defined as the ratio of the conductive heat resistance within the object to the convective heat transfer resistance across the object's boundaries.

2.1.3. Velocity autocorrelation function (VAF)

Let $A(t)$ and $B(t)$ represent two time dependent signals (or waves) and define the time correlation function $C(t)$ by

$$C(t) = \lim_{\tau \to \infty} \frac{1}{\tau} \int_0^\tau A(t_0) B(t_0 + t) dt_0 = \langle A(t_0) B(t_0 + t) \rangle \qquad (2.1.6)$$

This integral represents an average accumulated over time from t_0. A is sampled at the time origin and B is sampled after a delay time t. Thus, $C(t)$ depends on the length of the delay. When A and B are different quantities, $C(t)$ is called cross-correlation function. When A and B are the same quantity, $C(t)$ is called autocorrelation function. For example, considering a system of N particles and VAF at t=0 is calculated as

17

$$C(t=0) = \frac{1}{N} \sum_{1}^{N} (v_i(t=t_0).v_i(t=t_0)),$$ and for the subsequent time step as

$$C(t=n\Delta t) = \frac{1}{N} \sum_{1}^{N} (v_i(t=t_0).v_i(t=t_0+n\Delta t)).$$ The calculation stops after a fixed value

of n, and starts again to calculate another VAF, beginning at a new time origin. The final VAF is therefore an average of all the VAFs that have been calculated during the simulation. The result is usually plotted as a function of time. If each particle does not interact with each other in the system, its velocity will not change with time. That means all calculated VAF, $C(t)$, should be the same and the plot is a horizontal straight line. On the other hand, if the interaction between particles is weak but not negligible, i.e., in gas phase, the plot of VAF is an exponential decay, indicating the presence of weak forces slowly degrading the velocity correlation. In liquid or solid phase, each particle is strongly influenced by its neighbors. Its motion is therefore an oscillation around the equilibrium position. As a result, VAF in this case will oscillate between negative and positive values and slowly decays with time (Figure 2.1.1).
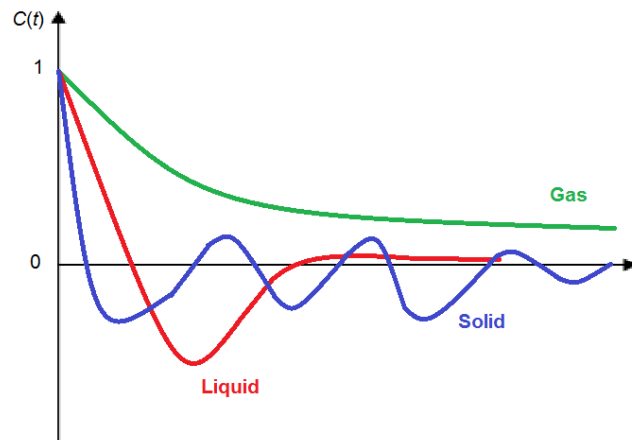
Figure 2.1.1. Plot of velocity autocorrelation function, $C(t)$, with time for gas, liquid and solid matters.

The velocity autocorrelation function (VAF), $C(t)$, is usually employed to calculate the vibrational spectrum or diffusive properties of system of atoms in MD simulations. The vibrational spectrum for the system can be calculated by taking the Fourier Transform (FT) of the VAF as

$$F(\omega) = \frac{1}{\sqrt{2\pi}} \int_{-\infty}^{\infty} \exp(i\omega t)C(t)dt$$

(2.1.7)

and the vibrational density of states (VDOS) is then

$$D(\omega) = F^2(\omega)$$

(2.1.8)

where ω is the vibrational frequency of an atom. Since the Kapitza resistance occurs due to the differences in electronic and vibrational properties of both sides forming the interface, the overlapping extent between VDOS profiles is a qualitative measurement of the vibrational coupling. Higher overlap would allow more efficient heat flow through such harmonic coupling and smaller Kapitza resistance.[27, 48, 54]

2.1.4. Green-Kubo relation

When a weak external field is applied to a system which is at equilibrium, the properties of that system will change linearly according to the external field. For example, Ohm's law states that the current I is linearly proportional to the applied voltage, V, as $I = \sigma V$. Similarly, the local heat flux q is linearly proportional to the temperature gradient as described in Equation (1.1.1). In general, the linear response theory (LRT) states that a current output function of time $S(t)$ will change linearly according to an input signal in the past, $F(t')$, as

$$S(t) = \int_{-\infty}^{t} dt' \chi(t - t')F(t')$$

(2.1.9)

where $\chi(t\text{-}t')$ is the linear response function. In the mid 1950's, Green and Kubo reported a mathematical expression for calculating transport coefficients in terms of integrals of time correlations. The linear transport coefficients, L, are exactly related to the time dependence of equilibrium fluctuations in the conjugate flux, $\vec{J}$, as

$$L = \beta V \int_0^\infty dt \left\langle \vec{J}(0)\, \vec{J}(t) \right\rangle \tag{2.1.10}$$

where $\beta = 1/k_b T$ (k_b is Boltzmann constant) and V is the volume of the system. Following this formalism, the thermal conductivity of a system can be calculated as

$$K = \frac{1}{Vk_b T^2} \int_0^\infty dt \left\langle \vec{J}(0)\, \vec{J}(t) \right\rangle \tag{2.1.11}$$

Using MD simulations together with Green Kubo relation provides a powerful approach to study thermal properties of CNTs and GSs. The first attempts to calculate K of CNTs/GSs were performed in 2000, [10, 55] and those results were validated by experimental measurement conducted almost ten years later. [11, 56] Furthermore, it is possible to compute the interfacial thermal conductance across the interface, G, which is the inverse of Kapitza resistance, with the Green-Kubo theory[57]

$$G = \frac{1}{Ak_b T^2} \int_0^\infty dt \left\langle Q(0)Q(t) \right\rangle \tag{2.1.12}$$

where A is area of the interface and Q is the total energy flux from a group of atoms A to another group of atoms B as

$$Q_{A \to B} = -\frac{1}{2} \sum_{i \in A} \sum_{j \in B} Q_{ij} = -\frac{1}{2} \sum_{i \in A} \sum_{j \in B} (\dot{\vec{r}}_i + \dot{\vec{r}}_j)\, \vec{f}_{ij} \tag{2.1.13}$$

Note that the expression in the above equation has the form of velocity multiplied by force, which equals the rate of work done. [57]

2.2. Monte Carlo simulations

A Monte Carlo (MC) method is a statistical approach that involves using random numbers and probability to solve problems. It was first developed by Von Neumann and Ulam in 1946 during the Manhattan Project, in the Los Alamos National Laboratory. Monte Carlo methods are often used in computer simulations of physical and mathematical systems. These methods tend to be used when it is impossible to compute an exact result with a deterministic algorithm.

For the case of heat transfer in nanocomposites, instead of treating the thermal transport in solids as a wave-like process, i.e. using phonons, the MC approach considers the heat flow to be the result of the movement of discrete heat walkers that travel through the material by Brownian motion.[58] Similar algorithms have been used for the simulation of heat or mass transfer in convective flows[59-61] and in porous media [61, 62]. Based on Einstein's Brownian motion theory [63], at each time step, the walkers move through the matrix with random jumps that are evaluated in each space direction by drawing random numbers from a normal distribution with a zero mean and a standard deviation, σ, given

$$\sigma = \sqrt{2D_m \Delta t} \tag{2.2.1}$$

where D_m is the thermal diffusivity of the matrix material and Δt is the time increment of the simulation. Because a heat walker is not allowed to jump across the CNTs within one time step, the value of Δt should be small enough to satisfy $\sigma < R$, the radius of a CNT. Once a thermal walker arrives at the matrix-inclusion interface, it can either enter the inclusion based on a probability, designated as f_{m-i}, or remain in the matrix with a

probability $(1-f_{m-i})$. Note that the physical meaning of this probability is the average phonon transmission probability, which is described in Equations (1.2.2) and (1.2.3).

Once a walker moves inside an inclusion, it is assumed to distribute randomly and uniformly inside the inclusion, because the thermal conductivity of the inclusion (be it a CNT or a GS) is about four orders of magnitude larger than the thermal conductivity of the matrix. In every subsequent time step, the heat walker can exit the inclusion based on another probability, designated as f_{i-m}, that determines whether the walker will exit or will remain inside the inclusion, in which case it will be re-assigned a new position inside the inclusion randomly. Based on thermal equilibrium, and assuming that the Kapitza resistance is the same when entering and when exiting the inclusion, the probabilities f_{m-i} and f_{i-m} are related as follows:

$$V_i \, f_{i-m} = C_f \, \sigma A_i \, f_{m-i} \tag{2.2.2}$$

where A_i and V_i are the surface area and the volume of the inclusion, respectively, and C_f is a thermal equilibrium factor, which depends on the inclusion's geometry and needs to be determined empirically.[64] As a heat walker exits the inclusion, it performs a random jump into the matrix or into another neighbouring inclusion.

2.2.1. Generating the inclusions inside the computational box

As discussed in Chapter 1, the accuracy of calculating K_{eff} depends strongly on how realistic it is for the algorithm to be able to generate the CNTs and GSs inside the computational box.

In order to create a randomly oriented thin parallelepiped, representing a perfect GS, one needs to generate three different random angles corresponding to the rotation of the GS axis in the three directions of the Cartesian coordinate system. If the GS is

required to be placed parallel or perpendicular to the x-axis (i.e., the axis parallel to the direction of heat flux), one can simply set the corresponding angle to be zero or $\pi/2$, respectively. For the case of a straight rod, representing a perfect CNT, there are only two random angles required to generate randomly oriented cylinders. By changing the initial seed number used for the random number generator, the placement and orientation of the inclusions can be changed randomly.

The configuration of CNTs and GSs in polymer matrix is not such that they are perfectly straight and uniformly dispersed. Instead, they can be twisted and bended into worm-like geometries and stacked together into bundles.[41, 65, 66] The following algorithm was developed to generate the worm-like CNTs in 3D. Each CNT is composed of the same number of segments, noted as N. Each of these segments is a straight solid cylinder. The length of each cylinder is noted as Δs and its radius is noted as R. The contour length of a CNT, noted as L, is equal to the segment length multiplied by the number of segments, while the end-to-end length of a CNT is noted as L_e. In order to make a continuous and smooth CNT, we create solid spheres with the same radius at the junctions between two neighboring CNTs, as seen in Figure 2.2.1. The worm-like geometry of one CNT was created by first generating a random straight solid cylinder, noted as segment 1, inside the computational box. The placement and orientation of the first segment is random. The second segment is created at the end of the first segment. However, the relative angle between the second and the first segment, θ_k, is not a random number between 0° and 360°, but it is $0 < \theta_k < \theta_{critical}$, instead. The critical angle, $\theta_{critical}$, is defined as the angle that the CNT is allowed to be bended without buckling [67-69]. This angle is a function not only of the CNT properties

(radius and aspect ratio) but also of the surrounding environment [70]. The third

segment, and each segment thereafter, is generated with the same scheme. Note that

there are two angles, the inclination angle, ϕ_k, and the azimuth angle, φ_k, that control the

orientation of each segment in 3D, and $\phi_{critical}$ and $\varphi_{critical}$ are defined in the same way as

$\theta_{critical}$ (Figure 2.2.1). The two angles are, thus, generated for each new segment as ϕ_{k+1}

$=\phi_k + \text{rand}(0,\phi_{critical})$ and $\varphi_{k+1} = \varphi_k + \text{rand}(0, \varphi_{critical})$. After the first CNT is created, the

2nd CNT is randomly placed inside the box in such a way that it does not overlap with

the previous one.
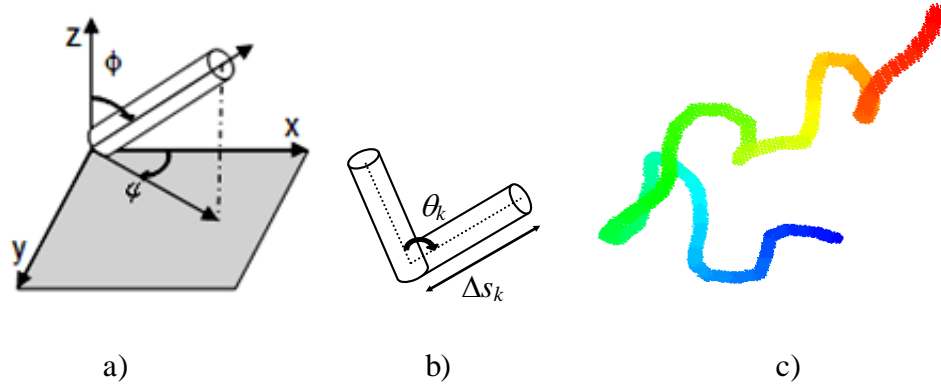
Figure 2.2.1. a) The orientation of a segment is defined by two angles, ϕ and φ, b) the relative angles between segment k and the next one is noted as θ_k, c) a realistic geometry of one CNT in 3D is constructed by controlling ϕ_{critical} and $\varphi_{\text{critical}}$. Relative angles between 2 segments are random numbers ϕ_k, φ_k that satisfy $0<\phi_k<\phi_{\text{critical}}$ and $0<\varphi_k<\varphi_{\text{critical}}$, respectively.

The stiffness of a filament (i.e., CNTs, fibers, polymer chains) is related to its persistence length L_p, which is calculated as [71]

$$L_p = \frac{L^2}{(N-1)^2 \pi^2 \, \text{var}(a_n)} \tag{2.2.3}$$

where $\text{var}(a_n)$ is the variance of the mode amplitude of the N-1 components that are obtained when the nanotube shape (*i.e.,* the tangent angle of the nanotube) is decomposed in Fourier modes. The mode amplitude coefficients are approximated as

$$a_n \cong \sqrt{\frac{2}{L}} \sum_{k=1}^{N} \theta_k \Delta s_k \cos(\frac{n\pi}{L} s_k^{mid}), n = 1,..., N-1 \tag{2.2.4}$$

$$s_k^{mid} = \Delta s_1 + \Delta s_2 + ... + \Delta s_{k-1} + 0.5\Delta s_k \tag{2.2.5}$$

Above, L is contour length, Δs_k is the length of segment k, N is the number of segments, and θ_k is the relative angle between two continuous segments. Hence, the filament can be considered as rigid when $L \ll L_p$. It can bend significantly when $L \gg L_p$ or it can be

25

semi-flexible when $L \approx L_p$. As already mentioned, the persistence length of CNTs has been reported to cover a wide range of values, from hundreds of nm up to hundreds of μm. Note that the methods employed to measure L_p could not distinguish between single-walled CNTs and small bundles [70, 72-74]. In our algorithm, $\Delta s_k = \Delta s = $ constant. By varying the critical angles between each segment, $\phi_{critical}$ and $\varphi_{critical}$, one can generate CNTs with different degrees of bending/twisting or, in order words, different values of L_p (Figure 2.2.1). For each simulation, the mean and variance of L_p are computed in order to control the geometry of CNTs. As a result, the pre-processing step of generating the configuration of CNTs inside the computational box is completed. The configuration of CNTs in this work is similar to those SEM images reported by Lee *et al.* [66, 75].

a)   b)
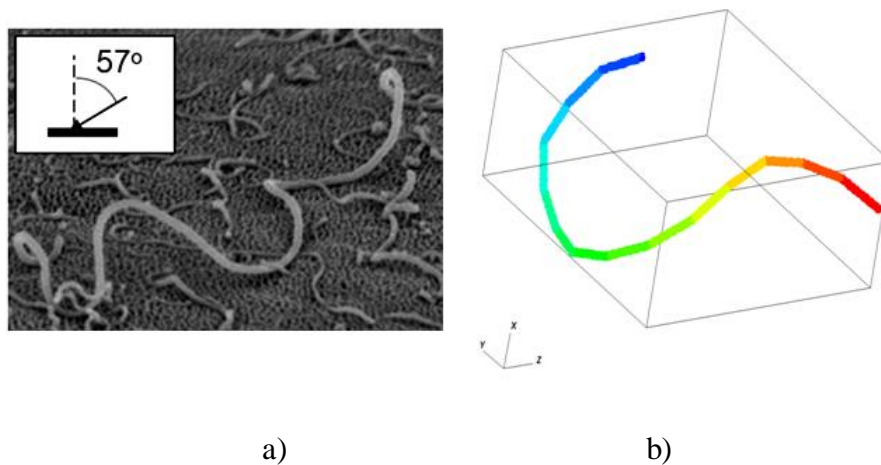
Figure 2.2.2. a) SEM image of MWCNTs on ceramic filter (side view), adapted from Lee *et al.*[75] . The angles indicate the observation positions from the vertical line. b) One worm-like CNT (contour length of 450nm, end-to-end length of 180nm, persistence length of 100nm) consisting of 15 segments (in different colors) is generated inside a computation box of 450x200x200 grid.

2.2.2. Equilibrium simulations

The thermal equilibrium factor, C_f, appearing in Equation (2.2.2) was obtained as follows: First, a single CNT was placed randomly inside a rectangular computational box of 450 x 200 x 200 grid points. Second, heat walkers were released at every grid cell and were allowed to perform their random walk. The fraction of heat walkers inside the CNT over the total number of heat walkers, noted as walker density, was calculated after increments of 500 time steps and the simulation was stopped once this value did not change more than 10% with simulation time. This was the equilibrium state. The correct value ($C_f = 0.35$) was considered to have been reached when the volume fraction of the CNT was equal to the fraction of heat walkers that was inside the CNT (Figure 2.2.3 b).
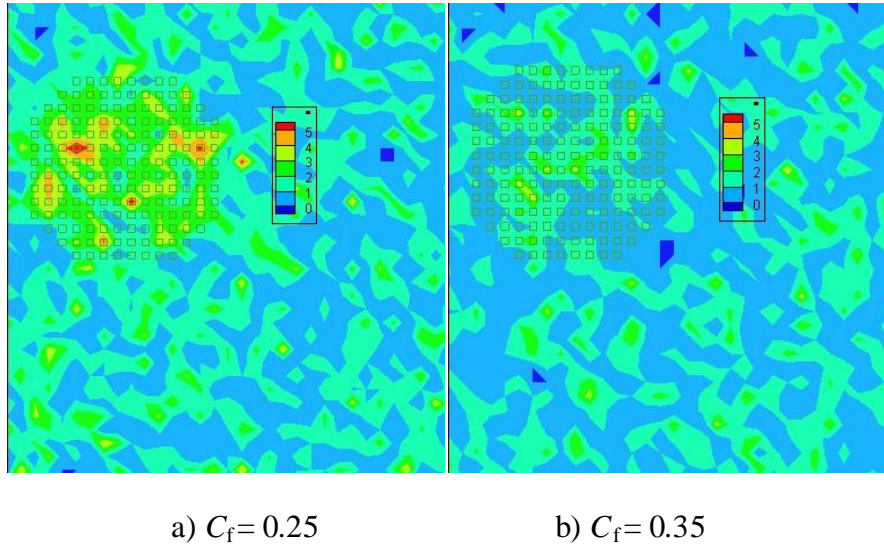
a) $C_f = 0.25$ b) $C_f = 0.35$

Figure 2.2.3. A slice through the computational box containing one CNT during equilibrium simulations. The density of heat walkers is plotted when a) $C_f = 0.25$ and b) $C_f = 0.35$. The correct value of $C_f = 0.35$ results in similar walker density between the CNT (in cubic grid) and the rest of the computational box.

A similar procedure was employed to compute C_f for a GS: first, one parallelepiped (representing a large GS) having dimensions of 2.52nm x 64.45nm x

27

0.34 nm was placed randomly inside a cubic computational box with sides equal to 100nm (300 x 300 x 300 grid points). Second, the heat walkers were released at every grid cell and were allowed to perform their random walk. The fraction of heat walkers inside the GS was calculated after increments of 500 time steps and the simulation was stopped once this value did not change any longer with simulation time (equilibrium state). The correct value of the equilibrium factor of the GS ($C_f = 0.33$) was considered to have been reached when the volume fraction of the parallelepiped was equal to the fraction of heat walkers inside the parallelepiped. Because there is one heat walker released at every grid cell at the beginning of the simulation, the number of heat walkers in each GS at equilibrium has to be equal to the number of grid cells constituting the GS or, in other words, the fraction of walkers staying inside the GS must be equal to the volume fraction of GS at thermal equilibrium conditions. Lastly, this value for C_f was checked further by placing 88 parallelepipeds (2.52nm x 64.45nm x 0.34 nm) randomly inside the same cubic computational box and examining the fraction of heat walkers inside each GS as compared to the expected value of this fraction. At thermal equilibrium, the heat walkers should distribute uniformly and the theoretically expected value of the fraction of the walkers inside all the GS should be equal to the volume fraction of the GS. Figure 2.2.4 is a plot of the fraction of walkers inside each of the GS sheets in this case.
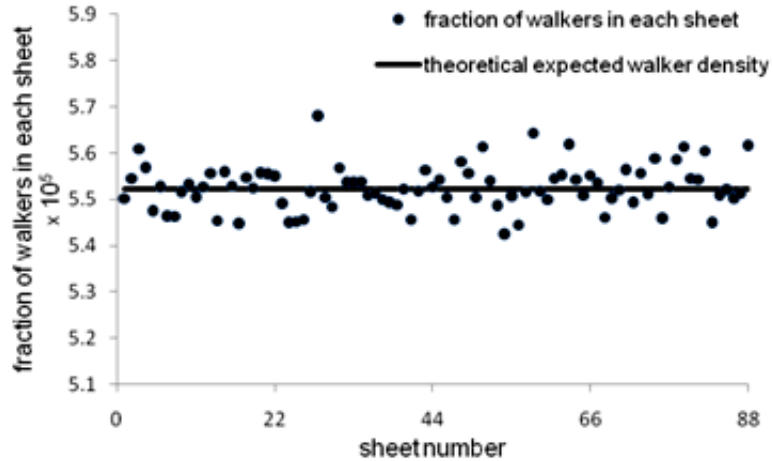
Figure 2.2.4. Fraction of walkers inside each GS with the sheet number (theoretically expected fraction of walkers) at thermal equilibrium state and $C_f = 0.33$. There are 88 sheets (2.52nm x 64.45nm x 0.34 nm) that are randomly dispersed inside a cubic computational domain with sides of 100 nm, so the fraction of the walkers within each sheet is expected to be equal to the volume fraction of one sheet (2.52 x 64.45 x 0.34 / 1,000,000 = 5.52×10^{-5}). Because there is one heat walker released at every grid cell, the number of heat walkers in each GS at equilibrium will be equal to the number of grid cells constituting the GS or, in other words, the fraction of walkers staying inside the GS must be equal to the volume fraction of GS at thermal equilibrium conditions.

2.2.3. Isoflux simulations

During isoflux simulations, thermal walkers were released from one side of the computational domain, at $x = 0$, representing the release of heat from a heated surface. At the same time, an equal number of cold walkers were released from the opposite plane, representing a cooled surface. To save computational time, the trajectories of these cold walkers were considered to be mirror images of the trajectories of the hot walkers. The time step was equal to 10^{-4} sec. The boundaries in the other two space directions were periodic. This scenario corresponds to the case of having a constant heat flux throughout the domain, and the temperature profile should be a straight line with a slope inversely proportional to the thermal conductivity of the composite.[8] The temperature was obtained by counting the number of heat walkers in each grid cell after

attaining steady state conditions, and subtracting the number of heat walkers originating from the cold side of the box from the number of heat walkers originating from the hot side of the box (Figure 2.2.5). [76] The same procedure was implemented for the pure matrix, without any inclusions present, and for nanocomposites with varying amounts of inclusions.

The ratio between the temperature gradients without (i.e, when only the matrix was present in the domain) and with the inclusions is reported as the effective thermal conductivity of the nanocomposite divided by the thermal conductivity of the matrix (K_{eff}/K_m). Following this procedure, six different simulation runs were conducted to obtain results for the conditions of each numerical experiment. The error bar representing the standard deviation of the results was calculated using Student's t-test with 95% level of confidence.
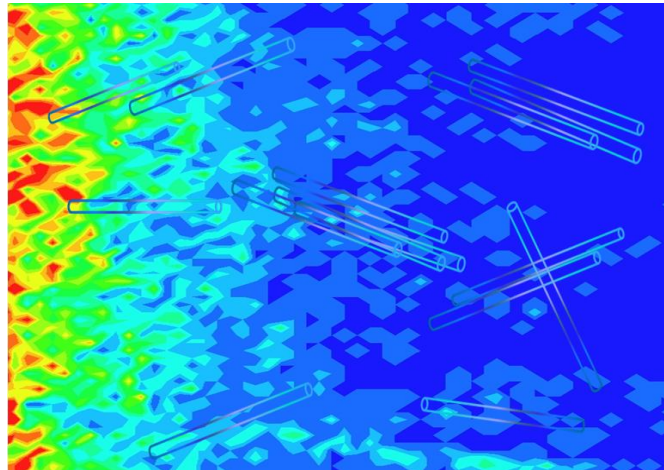
Figure 2.2.5. A contour plot of heat walkers during isoflux simulation for system of CNTs-polymer composite. The hot walkers were released on the left side and cold walkers were released on the opposite side. The temperature gradient was obtained by counting number of walkers in each grid unit when the system attained the steady state.

Chapter 3: Effective Heat Transfer Properties of Graphene Sheet Nanocomposites and Comparison to Carbon Nanotube Nanocomposites[*]

3.1. Introduction

Carbon nanotubes with their outstanding electrical, thermal and mechanical properties have been suggested as reinforcement fillers in a variety of composite materials. By incorporating CNTs into a polymer matrix, or by dispersing CNTs into a solution, the effective thermal conductivity of the resulting composite can be increased. For example, this enhancement has been found to be from 80% to 125% at 1 wt% over pure polymer for the case of epoxy composites,[78] or by a factor of almost 4 in the case of high volume fraction single-walled carbon nanotubes (SWNTs) in polystyrene.[41] Based, however, on the properties of pure CNTs, one would expect a much higher increase of the effective thermal conductivity of such composite materials, up to an order of magnitude according to the classical theory of Maxwell. The presence of resistance to heat transfer at the CNT-polymer interface, known as the Kapitza interfacial thermal resistance, is the reason for this difference.

The value of Kapitza resistance can be roughly estimated by the acoustic mismatch theory,[6] which attributed this resistance to phonon transport across the interface of dissimilar materials, as discussed in Chapter 1. The overall effective thermal conductivity of a system with nanoinclusions depends on the volume fraction of the nanoinclusions and on the interfacial thermal resistance. It has been suggested that the effective medium theory can provide insights about the thermal behavior of such

---

systems[33], by taking into account the Kapitza resistance and different geometries of nanoinclusions. The effective thermal conductivity, K_{eff}, of CNT nanocomposites can also be calculated numerically with Monte Carlo-based methods, following the approach developed by Duong *et al*.[58] This method offers the advantage of explicitly accounting for the random or controlled placement of the CNTs within the matrix, the Kapitza resistance between the CNTs and the matrix, and even the presence of a thermal boundary resistance between neighboring CNTs in contact with each other.[79, 80] This method has been validated by comparisons to experimental data,[64] and it has also been used to estimate the Kapitza resistance effects for suspension systems.[81, 82]

The nature of interfacial thermal resistance at the atomic scale can be explored with molecular dynamics (MD) simulations.[83-85] It has been reported that the overlap of the thermal vibrational spectra between two materials is the key point to control the Kapitza resistance at the interface.[22, 86] Multiscale modeling, in which the Kapitza resistance is examined by atomic-scale simulations and a meso/macroscopic approach is employed to study the thermal properties of bulk materials, can be seen as a suitable approach to this problem. Clancy *et al*.[84] employed molecular dynamics simulations together with effective medium theory to study the effect of functionalization on Kapitza resistance and thermal conductivity of resulting nanocomposites. They concluded that functionalization of edges and faces of nanoparticles is modestly effective in improving the thermal conductivity of the composite.

Graphene sheets (GS) have attracted attention because they are both cheaper[87] and possess properties analogous to those of CNTs[88-90]. Balandin *et al*.[56] reported extremely high values of the thermal conductivity of single-layer GS that outperform

CNTs in terms of heat conduction. This result gives rise to the expectation that GS composites might be able to fulfill the promise of thermally conductive carbon-based nanocomposites. Recent theoretical and experimental investigations[91] suggest that electronic and magnetic properties of nano GS ribbons are strongly dependent on the edge structure. Molecular dynamics simulation studies investigated the thermal conductivity of graphene sheets with different edge terminations, and with different shapes. It was found that graphene nanoribbons have outstanding ballistic transport properties[12, 92] and nanoribbons with zigzag long edges possess 125% higher thermal conductivity than that of armchair edges.[93, 94] When CNT and GS are dispersed in organic mediums, the nanocomposite thermal conductivity will be affected by the Kapitza resistance. To minimize the Kapitza resistance, it has been suggested that functional groups, like alkane chains, should be covalently bonded to CNTs or GSs.[95-97]

While MD simulations have answered the question of whether GS has less Kapitza resistance than CNT or not,[86] the question of how much the macroscopic thermal properties of resulting nanocomposites are affected by the Kapitza resistance remains unanswered. In this chapter, we investigate the effective conductivity of GS nanocomposites by means of mesoscopic, off-lattice Monte Carlo simulations. In addition to the presentation of a computational methodology for the study of the macroscopic effects of GS orientation, dispersion and volume fraction on the effective thermal conductivity of GS nanocomposites, the contributions of this chapter are: (a) a comparison of the macroscopic thermal performance between CNT nanocomposites, GS nanocomposites and functionalized-GS nanocomposites, and (b) the utilization of

33

this methodology to calculate the Kapitza resistance of GS in polystyrene composites from recently conducted experiments. However, because of the coarse-grained level of description adopted herein, edge effects cannot be addressed.

3.2.   Simulation methodology and selection of simulation parameters

In the present work, instead of placing the walkers at the CNT-matrix interface before moving them out of the CNT,[58] the exiting walkers are randomly placed inside a shell whose outer surface is the inclusion-matrix interface. The thickness of this shell is determined by the standard deviation of the Brownian motion movement, equal to 2σ (see Equation (2.2.1)). The walkers jump out of the inclusion after being placed randomly inside that shell (see Figure 3.2.1). For the GS, which is very thin, the walkers jump out from their locations inside the GS without first being moved to the inclusion surface. This scheme results to a uniform and continuous distribution of the walker density inside and outside the inclusions, even across the interface, at conditions of thermal equilibrium. In prior versions of the algorithm,[58] there was a discontinuity of the walker density across the interface at thermal equilibrium conditions, which was incorporated into the value of C_f. The new algorithm is, therefore, physically more reasonable.
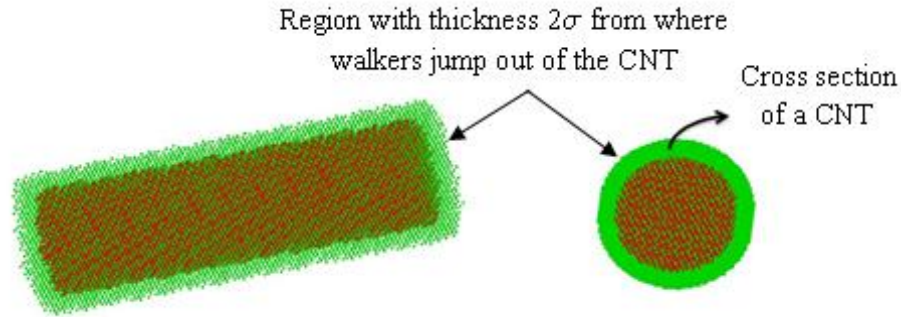
Figure 3.2.1. The thermal walkers can jump out of the inclusions by first arriving in a shell close to the inclusion-matrix interface (green area). This type of algorithm is computationally more efficient than letting walkers try to exit from anywhere inside the inclusion, and at the same time ensures a continuous and uniform distribution of the walkers across the interface at thermal equilibrium.

The numerical methodology for calculating the thermal equilibrium factor, $C_f =$ 0.35 and 0.33 for CNTs and GSs, respectively has been described in Chapter 2. In order to estimate the effective thermal conductivity of a CNT or a GS nanocomposite, a cubic computational domain with sides of 100 nm and 300x300x300 equally spaced grid points was utilized. While the CNTs were simulated as solid cylinders, the GSs were considered as rectangular sheets, resembling GS nanoribbons. The thickness of the GS was equal to the distance between two graphene layers in graphite, which is 0.34nm,[98] and the radius of the CNTs was 0.4nm. Both the CNTs and the GSs were placed randomly inside the domain, with either random or controlled orientation relative to their axes, and were not in contact with each other (Figure 3.2.2). Isoflux simulations were performed to calculate K_{eff}/K_m and details of this procedure have been described in Chapter 2. Following this procedure, six different simulation runs were conducted to obtain results for the conditions of each numerical experiment. The error bar that appears in Figure 3.3.1–Figure 3.3.4 represents the standard deviation of the results calculated using Student's t-test with 95% level of confidence.

35

a)

b)
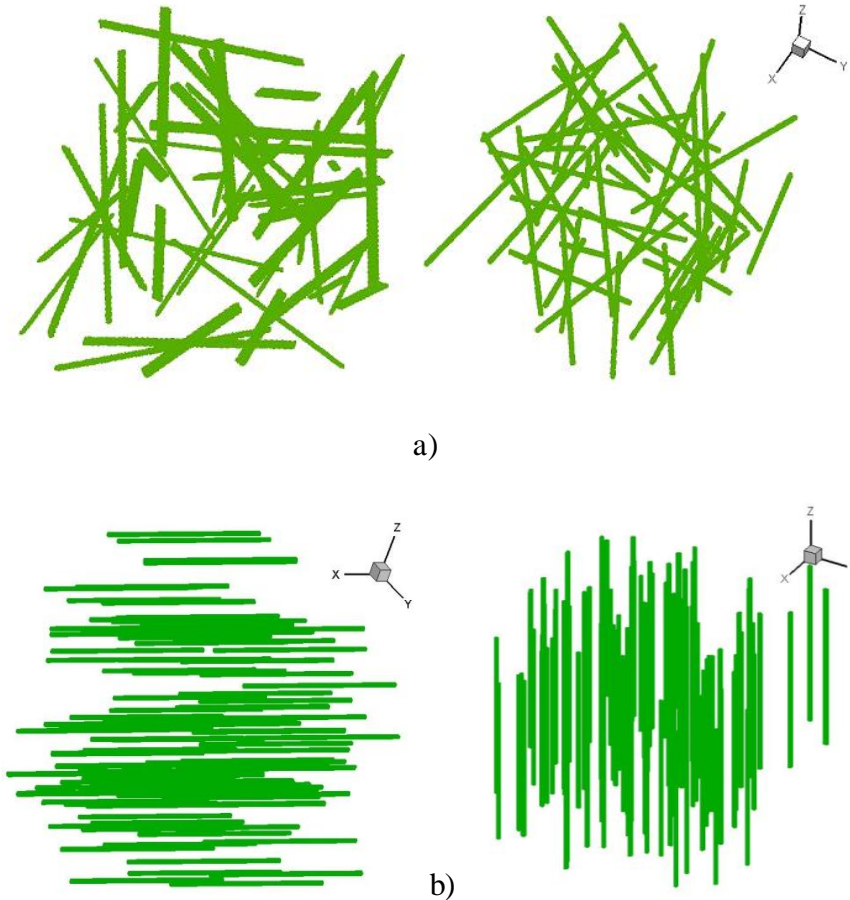
Figure 3.2.2. a) 50 GSs (2.52nm x 64.45nm x 0.34nm), left panel, and 50 CNTs (diameter = 0.8nm, length = 64.45nm, aspect ratio L/d = 80.5), right panel, that are randomly placed with random orientation inside a cubic computational domain with sides of 100 nm. (b). 100 CNTs (diameter = 0.8nm, length = 64.45nm, aspect ratio L/d = 80.5), right panel, that are placed parallel and perpendicular to the direction of heat flux (also x-direction) inside a cubic computational domain with sides of 100 nm.

The value of the Kapitza resistance is a required input for the simulation. One can either estimate the Kapitza resistance based on a simplified theoretical approach (such as the acoustic mismatch model, AMM, or the diffuse mismatch model, DMM), or obtain it from experiments, or from MD simulations. It is also possible, if experimental values of the effective thermal conductivity of the nanocomposite are known, to use MC simulations in order to back-calculate the Kapitza resistance for the nanocomposite. In the latter case, different values of the Kapitza resistance are

assumed, the simulation is run for each case, and the correct Kapitza resistance is the one that yields results in agreement between the experiments and the simulations. Conventional numerical methods, like finite elements, have been used to obtain the conductivity for GS with a trial and error procedure when temperature data are available experimentally,[35] but the value of the Kapitza resistance cannot be obtained. When K_{eff} of a composite is studied, with our particle-based and meshless algorithm, there is no need to generate a mesh that would fit the complicated geometry of inclusions dispersed into a matrix material, and to repeat the mesh generation every time a new configuration is examined. Furthermore, the incorporation of the Kapitza resistance at the interfaces happens in a natural way, through a probability, is one way to describe the Kapitza resistance (see Equation (1.2.2)).

Table 3.2.1. Properties and Kapitza resistance of SWNT and GS with and without functional groups in octane. The Kapitza resistance was calculated based on the acoustic mismatch (AMM) and the diffuse mismatch (DMM) model and with molecular dynamics simulations.[6, 49, 50, 99-101]

Composite	SWNT-octane	GS-octane	FGS-octane
$R_{bd}x10^8$ (m^{2}K/W)			
AMM	1.32	5.33	_
DMM	0.11	0.21	_
MD	4.26	1.33	0.42
	SWNT	GS	Octane
K (W/mK)[56]	3000-3500	4840-5300	0.124
Properties at 25°C	heat capacity (J/kgK)	velocity of sound (m/s)	density (kg/m^3)
Octane	2230	1171	710
SWNTs	670	17500	1400
GS	_	20000	2230 (graphite)

Table 3.2.1 is a summary of the theoretical predictions for the values of the Kapitza resistance for a CNT-octane and a GS-octane suspension system. Suspensions in octane were chosen because MD simulation results are available for CNTs, GSs and functionalized GSs (FGS) in such systems.[49, 50] Because of computing power

limitations, the MD simulations considered small GSs of $54 - 216$ carbon atoms and FGS were obtained by attaching single or double alkane chains at the edges of these GSs. As can be seen in Table 3.2.1, not only do the AMM and the DMM approaches yield different values for the Kapitza resistance, but their predictions also differ from those obtained from MD calculations. The AMM can provide an estimate, but not a precise value of the Kapitza resistance, because it does not take into account phonon scattering events at the interface. The DMM assumes that all the phonons are diffusely scattered at the interface, or, in other words, the incident phonon forgets where it came from and scatters in both media with the same energy. This diffuse scattering significantly decreases the Kapitza resistance at the interfaces, where the dissimilarity between two materials is extremely large. These theories cannot predict the Kapitza resistance for the case of functionalized GS, since the material properties appearing in Equations (1.2.1)-(1.2.3) are properties for pure substances. In light of these differences, and the difficulty to obtain theoretical predictions for functionalized GS, Kapitza resistance values inspired by MD simulations were used as input for the CNT-matrix, GS-matrix and functionalized GS-matrix Kapitza resistances in the MC simulations. It should be pointed out here that MD results have also shown that the Kapitza resistance for GS systems depends on the GS size, so only comparisons to experiments will validate our assumptions. The average phonon transmission probability of SWNT-octane and GS-octane was calculated using Equation (1.2.3). Furthermore, the results of Konatham and Striolo[50] indicate that FGS can be dispersed in octane, providing justification to our assumption that functionalized GSs do not agglomerate. Assuming well-dispersed GS, GS-GS heat transfer resistances were not taken into account.

3.3.   Results and discussion

3.3.1.   Graphene sheet nanocomposites compared to carbon nanotube nanocomposites

For comparison purposes, the CNT and GS considered in our simulations have the same length. The width of one GS is equal to the perimeter of a CNT. The FGS is modeled as having the same geometric shape and dimensions as a GS, with only difference in the value of the Kapitza resistance. Furthermore, in our calculations, a single value for the Kapitza resistance was assumed to apply everywhere at the interface between the matrix and the nano-inclusion, neglecting the effects of different GS edge types on the effective thermal conductivity. The number of CNTs and GSs used in each simulation run are presented in Table 3.3.1. Note that the volume of one CNT is smaller than that of one GS, so more CNTs are needed in order to keep the same vol% as with GSs. In our simulations, the CNTs are considered as straight cylinders with diameter d= 0.8 nm and aspect ratio (length/width) = 80.5. By unfolding the CNTs, we obtained GSs with L/d = 25.6.

Table 3.3.1. Number of CNTs and GSs used in the simulation.

%volume	0.5	1.0	2.0	3.0	Length (nm)	Length/Width	A_i/V_i
No. of CNTs	155	310	620	930	64.45	25.6	5.03
No. of GSs	88	176	352	528	64.45	25.6	6.70

(a)

(b)

(c)
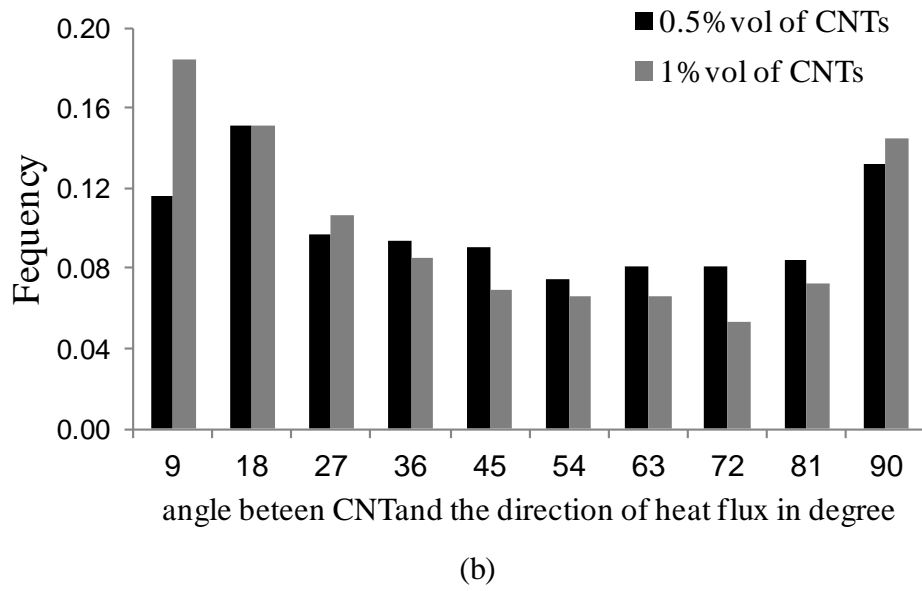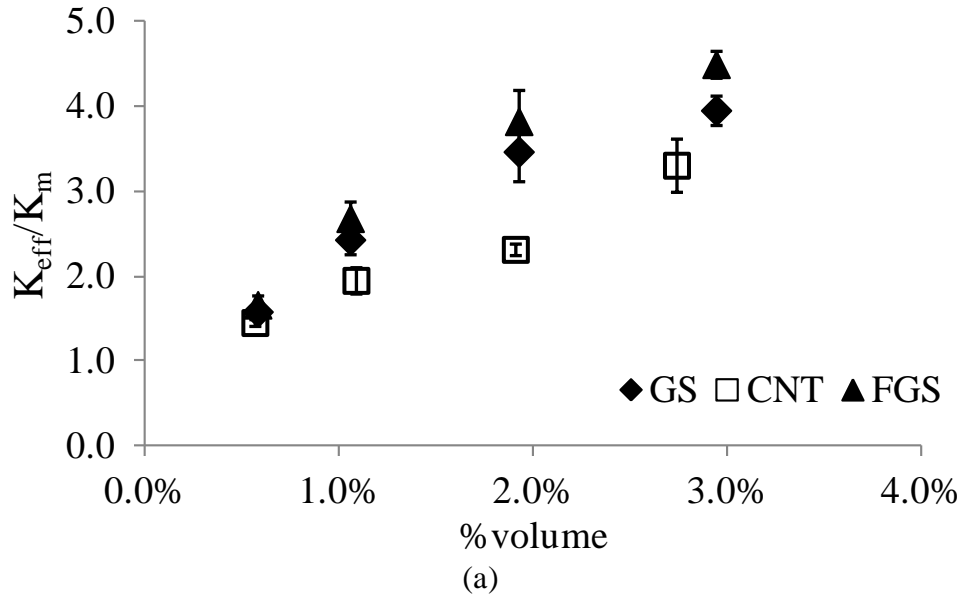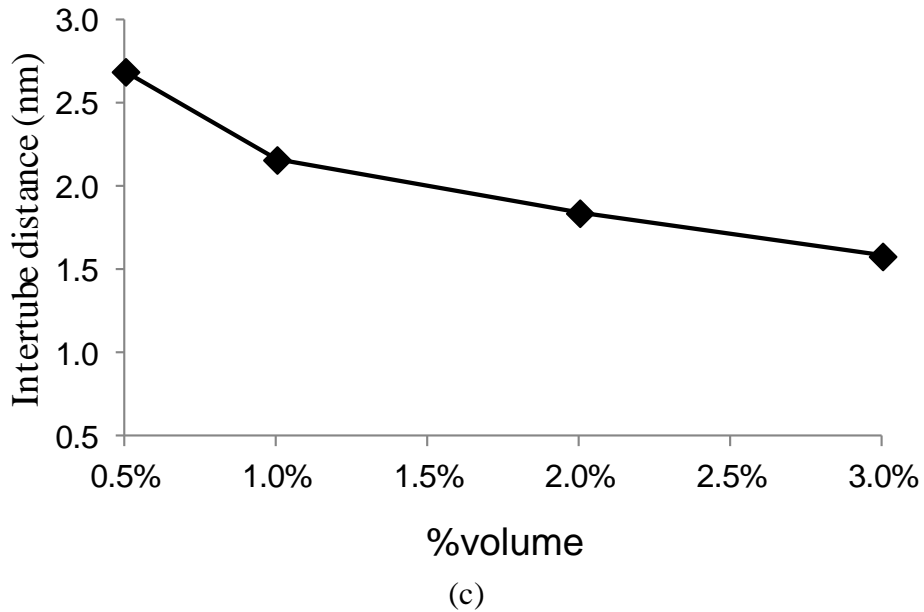
Figure 3.3.1. (a) Effective thermal conductivity of CNT composites (rectangles), GS composites (diamonds) and FGS composites (triangles) at various volume fractions. The inclusions are randomly placed with random orientation. The error bars indicate the variance of a student t-test with 95% level of confidence. (b) Distribution of the orientation of CNTs relative to the direction of the heat flux (i.e., x-direction). Zero degrees means the CNTs are parallel to x-direction and 90 degrees means the CNTs are perpendicular to x-direction. (c) Change of average distance between six closest neighbor CNTs with the amount of CNTs inside the composite.

The values of the effective thermal conductivity are presented in Figure 3.3.1a as a function of the volume fraction of CNTs, GSs and FGSs. The inclusions were randomly placed in the computational domain, and also had random orientation (i.e., a random angle of the CNT axis relative to the Cartesian coordinate system, and randomly oriented normal vectors to the GS planes). The inclusion placement algorithm worked sequentially, first randomly placing an inclusion and then checking whether this new inclusion intersected with previously placed inclusions. Also, for computational simplicity, neither GSs nor CNTs were allowed to intersect the faces of the computational box. Thus, despite the imposed random orientation, the distribution of

42

the angles is not exactly uniform, but it is symmetric. As shown in Figure 3.3.1b for CNTs, the distribution of the orientation angles for the lower volume fraction case is closer to being uniform. As detailed later, the CNT orientation affects the effective nanocomposite thermal conductivity. As it can be seen, GS composites exhibit higher values of K_{eff} than CNT composites. This improvement is more obvious at larger volume fractions, where the use of functionalized GS can provide over four times enhancement of the thermal conductivity of the matrix. Our predictions show a significant enhancement of the thermal conductivity for GS-based nanocomposites. This result is due to several facts. In our calculations the Kapitza resistance is assumed to be smaller for GS and FGS than for CNT; and the surface to volume ratio of one GS is 6.70, i.e., 33.3% higher than that of one CNT (Table 3.3.1).
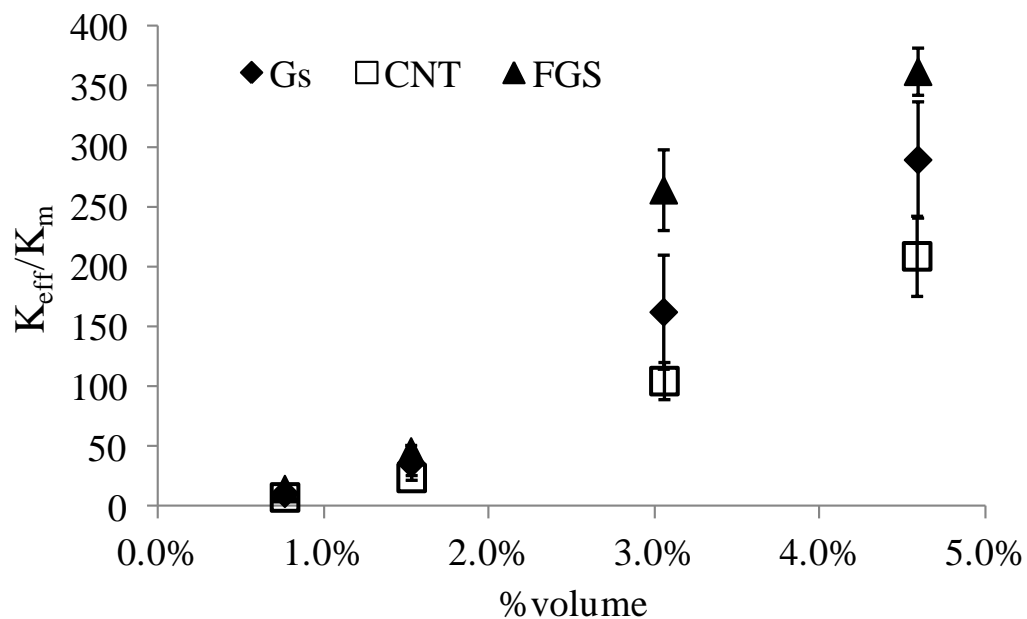
Figure 3.3.2. Effective thermal conductivity of CNT composites (rectangles), GS composites (diamonds) and FGS composites (triangles) at various volume fractions. The inclusions are randomly placed in the domain, but are aligned in the *x*-direction, so that they are parallel to the heat flux.

The values of K_{eff} for the case of randomly placed inclusions, but with their longest dimension oriented in the direction of the heat flux, are presented in Figure 3.3.2 as a function of the volume fraction of CNTs, GSs and FGSs. This is the case that yields the highest values of K_{eff}. With the same %vol, the effective thermal conductivity of GS composites is roughly 50% higher than that of CNT composites, while FGS composites are predicted to have K_{eff} up to twice that of CNT composites.

Results in Figure 3.3.1 and in Figure 3.3.2 suggest that K_{eff} of all nanocomposites increases as the inclusion (CNT, GS, or FGS) volume fraction increases. It should be pointed out that for the calculations discussed herein the nanoinclusions are well dispersed within the organic matrix. As the inclusion volume fraction keeps increasing, the average distance between the nanoparticles decreases (see for example Figure 3.3.1c for CNT composites), and the nanoparticles will eventually come in contact with each other. At those conditions, the nanoparticle-nanoparticle Kapitza resistance may become important, as suggested by Maruyama *et al.*[53], Zhong *et al.*[102] and Duong *et al.*[80].

The above results for CNTs are compared with results obtained from effective medium theory and the same volume fraction and size of the CNTs. Details of the analytical formulas have been described in Chapter 2.[33, 34] As seen in Table 3.3.2, the analytical results overestimate the effective thermal conductivity for the cylinders that are parallel to the heat flux and underestimate these values for the case of randomly oriented cylinders compared to the simulation results. The reason of this major discrepancy for cylinders parallel to the direction of heat transfer is that there exists a

Kapitza resistance at the interfaces at both ends of the cylinders when the cylinders are

parallel to the heat flux, but the analytical formula does not take into account this effect.

Table 3.3.2. Effective thermal conductivity of CNT-, GS-Octane and comparison with theoretical results[33, 34] at different vol%. The dimensions of CNTs are as described in Table 3.3.1. For the case of randomly oriented CNTs, the simulation generates truly random cylinders and the analytical formula considers aligned cylinders with an angle ϕ relative to the heat flux that satisfies $\cos^2\phi = 1/3$.

% volume	0.5	1.0	2.0	3.0
K_{eff}/K_m of CNT-octane				
Parallel, theory	121.96	242.92	484.85	726.77
Parallel, simulation	8.35	24.62	105.23	209.09
Random, theory	1.19	1.38	1.69	2.04
Random, simulation	1.44	1.94	2.30	3.29
Perpendicular, theory	1.01	1.02	1.04	1.06
Perpendicular, simulation	0.99	0.99	0.99	1.00
K_{eff}/K_m of GS-octane				
Parallel, theory	196.56	392.12	783.24	1174.35
Parallel, simulation	11.46	36.94	162.60	289.32
Perpendicular, theory	1.00	1.01	1.02	1.03
Perpendicular, simulation	0.99	0.99	0.98	0.99

3.3.2. Anisotropic heat transfer in nanocomposites with controlled morphology of

CNTs, GSs and FGSs

When the inclusions were perpendicular to the heat flux (Figure 3.3.3) our results predict no enhancement in the thermal conductivity in any of the cases examined. The values obtained for K_{eff} even decreased proportionally to the amount of inclusions placed in the system. The anisotropy ratio of the effective thermal conductivities of the composites with inclusions oriented parallel and perpendicular to the heat flux, (K_{eff-x}/K_{eff-z}, where K_{eff-x} and K_{eff-z} are the effective thermal conductivities in the direction of the heat flux and in the direction perpendicular to the heat flux, respectively), has values that are almost equal to K_{eff-x} , since K_{eff-z} is almost one for all cases. This anisotropy ratio represents the ratio of the largest to the smallest eigenvalue of the effective thermal conductivity tensor, often called the condition number of the tensor. As the inclusion volume fraction increases, the anisotropy ratio increases, reaching a value of over 350 for FGS and 4.5 vol%. It becomes evident that a material will behave as a thermally conducting material in one direction and as thermal shield in another, if the inclusions are properly oriented. Such properties would be possible to obtain with advanced CNT composites that have high volume fraction of oriented CNTs,[103, 104] but there is need for some experimental effort to produce nanocomposites with controlled orientation of the GS.
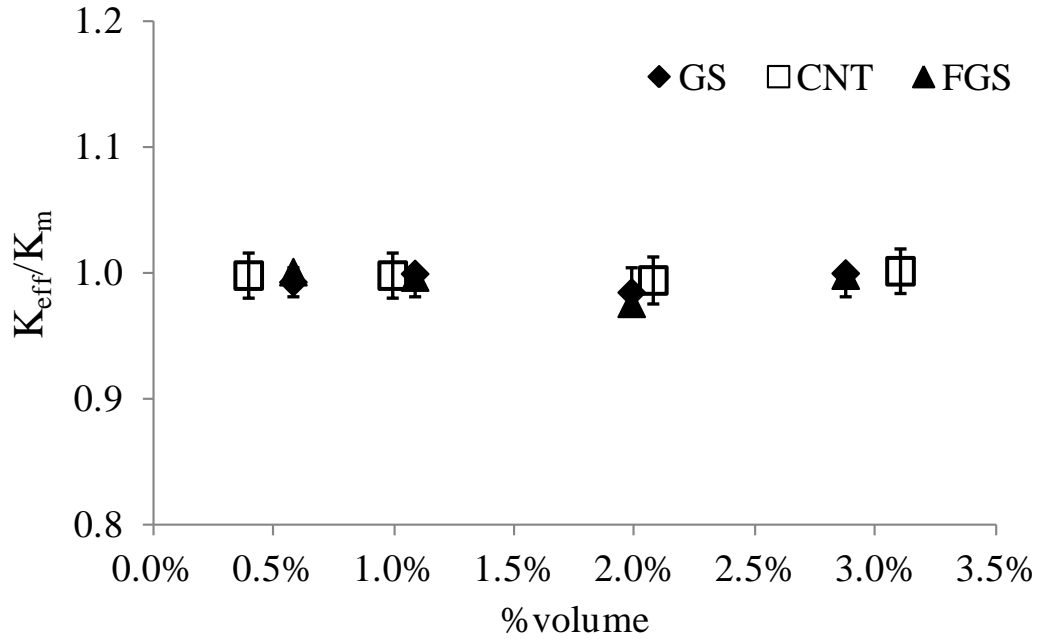
Figure 3.3.3. Effective thermal conductivity of CNT composites (rectangles), GS composites (diamonds) and FGS composites (triangles) at various volume fractions. The inclusions are randomly placed in the domain, but are aligned in the z-direction, so that they are perpendicular to the heat flux. For the GS cases, the plane of each GS is normal to the direction of the heat flux.

3.3.3. Effects of aspect ratio of CNTs and GSs

Each GS was considered as a rectangular sheet, in which the heat can travel along two directions parallel to the GS plane. On the contrary, the CNT was a cylinder that acted as an one-dimensional heat conducting inclusion, especially at high aspect ratios. In order to study this effect on K_{eff} of the composite, we simulated cases where the Kapitza resistance of the GS-matrix was set to be equal to that of the CNT-matrix resistance (as shown in Table 3.2.1). The simulations were performed at the same vol% (1.0%), with random inclusion orientation, but with different length/width ratios.
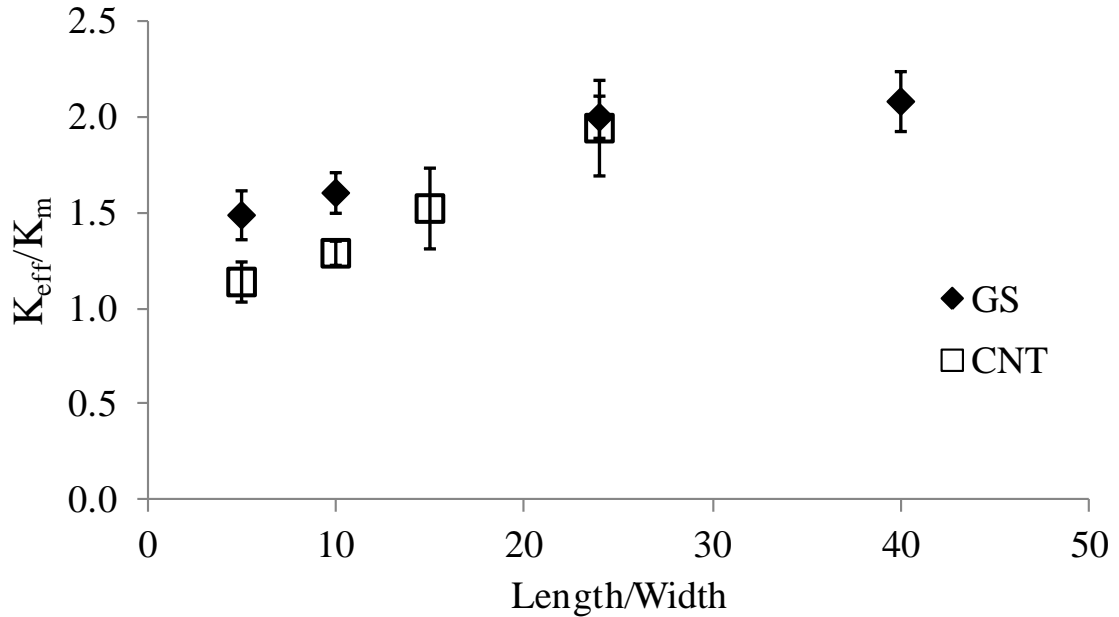
Figure 3.3.4. Effective thermal conductivity of CNT composites (rectangles) and GS composites (diamonds) at 1.0 vol% and different length/width ratios. The inclusions are randomly placed with random orientation.

As the length/width ratio (or length/perimeter ratio for the case of the CNTs) was equal to 25.6 for a GS and a CNT, no difference in K_{eff} of the composites was observed (Figure 3.3.4). At high length/width ratio, the width of the GS is rather small compared to its length, and the heat conduction along the length is dominant like that of the CNT. However, K_{eff} of GS composites is larger than that of CNT composites, when the width of the GS is comparable to its length, because the heat can travel along both directions in this case. Regarding the question of what type of composite would be more efficient for heat transfer, a CNT composite or a GS composite when the Kapitza resistance is the same for both, the answer depends on the length/width ratio (Figure 3.3.4). The value of K_{eff}/K_m increases as the length/width ratio increases from 5 to 25. Above this value, our predictions do not indicate enhancement of the effective thermal

conductivity for GS composites relative to CNTs. The inclusion type (CNTs or GSs) is only important in small length/width ratios.

It is also seen in Figure 3.3.4 that K_{eff} of both the GS and the CNT composites increases with increasing length/width ratio. It has been observed with the use of MD simulations [14] that K of both SWNT and GS is proportional to the length indicating purely ballistic heat conduction. Shiomi *et al.*[14] found that as the length of CNTs and GSs increases, the distribution of effective phonon mean free paths becomes broader, so that phonons with relatively long mean free paths cause an increase of the thermal conductivity. This also justifies our simulation approach to randomly and uniformly place the walkers once inside the inclusion, instead of moving them with Brownian movements, so long as the length of the nanoinclusions is larger than the phonon free path.

3.3.4. *Comparison to experimental results*

For CNT-based composites, validation of our protocol with comparison to experimental data has been described in our previous work[64, 81]. Kapitza resistances were estimated for CNT-epoxy ($R_{bd}= 4.01\times10^{-8}$ m^{2}KW^{-1}) and CNT-PMMA composites ($R_{bd}= 9.53\times10^{-9}$ m^{2}KW^{-1}). Based on experimental data of CNT-polyisoprene composites[105] at 1.0wt% (0.6vol%), Kapitza resistance was calculated ($R_{bd}= 8.14\times10^{-8}$ m^{2}KW^{-1}) by varying the value of f_{m-i} in the MC simulations until K_{eff} from the simulations matched the experiment. Using the Kapitza resistance thus obtained, we computed K_{eff} for CNT-polyisoprene composites at 5.0wt% (3.2vol%). As can be seen in Figure 3.3.5a, when the dispersion pattern of the CNTs is assumed to be the same at

1.0 and 5.0wt% CNTs within the nanocomposite, our MC simulations reproduce the experimental data even better than the effective medium theory from Nan *et al.*[33, 34].

A recent experimental report for GSs dispersed in polystyrene (GS-PS) at loadings less or equal to 2.0wt% substantiates the conclusion that GS nanocomposites are better thermal conductors than SWNT nanocomposites.[106] This report did not include an estimation of the Kapitza resistance at the GS-PS interface. However, by comparing the enhancement factor, K_{eff}/K_m, with our current work, we can obtain an estimate of the Kapitza resistance for the GS-PS system (Figure 3.3.5). For the same type of nano-inclusions and dispersion pattern, the ratio of the thermal conductivity of the composite divided by that of the polymer is affected by the Kapitza resistance rather than the type of the matrix material (polystyrene or octane). It is reasonable to conclude that composites with the same K_{eff}/K_m should have comparable Kapitza resistance, when the volume fraction of the inclusions and the dispersion pattern are the same.
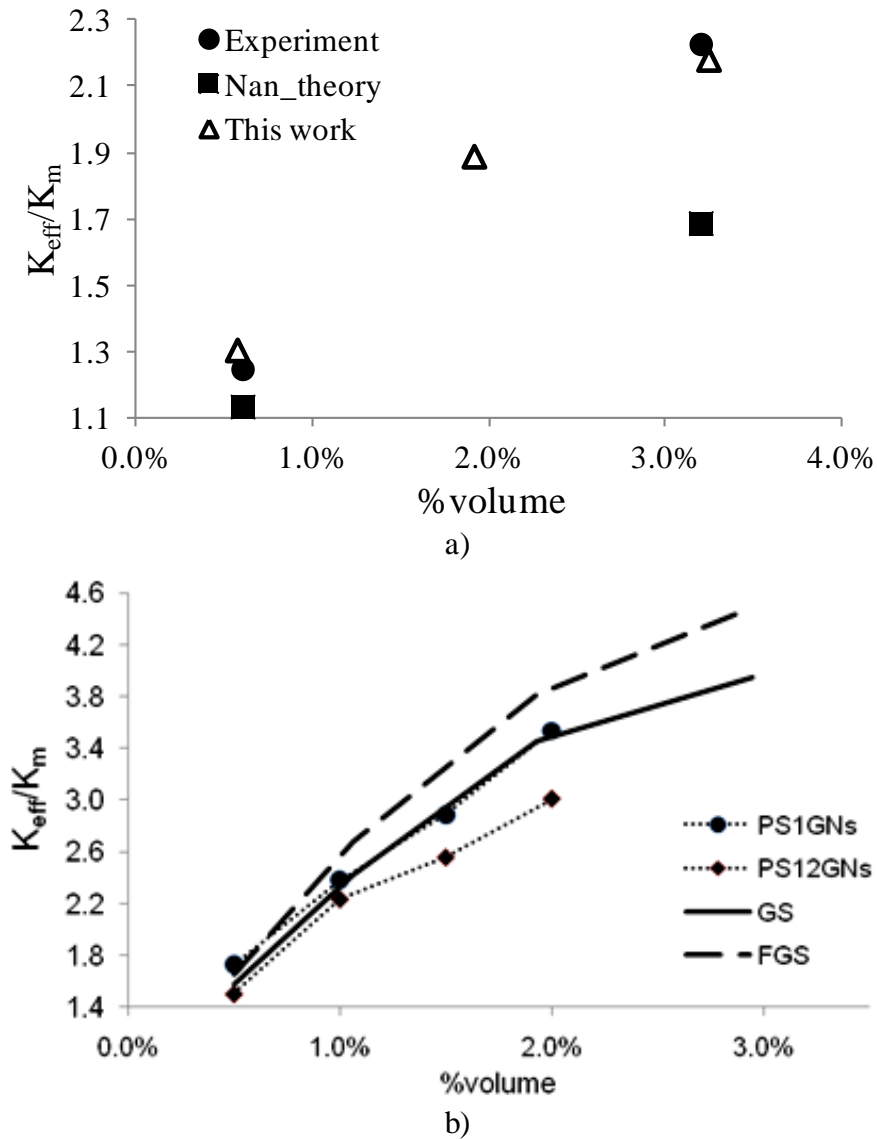
Figure 3.3.5. a) Comparison of the enhancement factor (K_{eff}/K_m) of CNT-Polyisoprene composite from experiment[105], Nan's theory[34] and this work. b) Comparison of the enhancement factor (K_{eff}/K_m) of GS-Octane (continuous line) and FGS-octane (dashed line) composites from this work with that of GS-PS composites from experiment (the designations PS1GNs and PS12GNs correspond to low grafting density and high grafting density samples, respectively, following the symbols in Fang *et al.*,[106]).

There is some uncertainty regarding the length/width ratio, the thickness and the dispersion pattern of the GSs used in the experiments, since the GSs can bend and even twist. However, based on Figure 3.3.4, we can see that the value of K_{eff}/K_m does not

change dramatically (28.5%) when varying the length/width ratio of the GSs. Assuming a pattern of randomly dispersed and randomly oriented GSs, we can see in Figure 3.3.5 that the experimental data from Fang *et al.*[106] for PS1GNs (i.e., GSs with very small fraction of PS grafting) have a similar enhancement factor to that of GS-octane for randomly oriented GSs of similar %wt in the present work. The value of Kapitza resistance of GS as well as FGS used in our work is 1.33×10^{-8} and 0.42×10^{-8} m^2KW^{-1}, respectively. The Kapitza resistance of GS-PS is, thus, comparable to that of GS-octane.

3.4.   Conclusions

In summary, using Monte Carlo methods, we have calculated K_{eff} of GS nanocomposites taking into account this Kapitza resistance, and we have found that they can become an alternative to CNT composites from both a financial and a technical point of view. Composites with functionalized GSs exhibit almost double K_{eff} relative to CNT composites for inclusions oriented it the direction of the heat flux. Furthermore, by comparison with experiment data[105, 106], we found that the Kapitza resistance for a CNT-polyisoprene and for a GS-PS system are 8.14×10^{-8} and 1.33×10^{-8} m^2KW^{-1}, respectively. The anisotropy ratio of the effective thermal conductivity tensor increases for GS nanocomposites, indicating that there is added value in pursuing the manufacturing of GS composites with controlled orientation of GS. Controlling the orientation of the GS in the composite can lead to the manufacturing of composites that have quite different thermal behavior in different directions. For example, for an anisotropy ratio of 350 (like the FGS case) the material can be a thermal insulator in one

direction and have a thermal conductivity 350 times larger than in a direction perpendicular to that. Finally, it appears that the two-dimensional heat transfer is not important for GS with an aspect ratio larger than 25, and that the most important factor that affects the effective thermal conductivity is the value of Kapitza resistance.

Chapter 4: Heat Transfer in High Volume Fraction CNT

Nanocomposites: Effects of Inter-nanotube Thermal Resistance[*]

4.1.   Introduction

Due to the high specific surface area of carbon nanotubes (CNT) (i.e., 1315 m^2/g for single-walled CNTs[108]), the transfer of heat in CNT-based composites is controlled by the thermal boundary resistance (also known as Kapitza resistance) at the nanotube-polymer interface. As a result of this resistance, while the electrical conductivity of SWNT composites has been reported to increase dramatically at percolation thresholds as low as 1.5wt%,[109] there is no radical enhancement of the thermal conductivity even above the percolation threshold. Can one bypass this poor performance by increasing the volume fraction of the nanotubes? Peters *et al.*[41] measured the effective thermal conductivity (K_{eff}) of single-walled CNT-polystyrene (SWNT-PS) composites at various temperatures above and below the glass transition temperature, and various weight fractions of SWNTs using differential scanning calorimetry. As the wt% of CNTs increased from 10.0 to 30.0%, K_{eff} of the composite was expected to increase by a factor of 3, but the measurements [41] showed an increase of ~ 15%. The reason for this behavior could be a poorer SWNT dispersion at high wt% and/or the presence of an additional thermal boundary resistance between the CNTs, when they are closely packed.

Currently available data from molecular dynamics (MD) simulations indicates that the CNT-CNT thermal boundary resistance can be higher than the thermal boundary resistance between a CNT and a polymer matrix.[102, 110] If in fact this is

---

[*] Most of the material presented in this chapter has been published in ref.[107] K. Bui, B. P. Grady, and D. V. Papavassiliou, Chemical Physics Letters 508 (2011) 248.

the case, then an increase in the volume fraction of CNTs in a composite will not improve its thermal properties, unless there are chemical bonds connecting adjacent CNTs[110]. Experimental evidence supporting such results is needed. In the present work, off-lattice Monte Carlo (MC) simulations were used to replicate the thermal behavior of the SWNT-PS composites of Peters *et al.*[41] at different volume fractions and at various temperatures. In addition to validating the simulation, the thermal boundary resistance between SWNT-PS and SWNT-SWNT was back-calculated by fitting the simulation results to the experimental data.

4.2.   Simulation setup

Details of MC simulations have been described in Chapter 2. An improved algorithm that is more accurate and computationally more effective for a heat walker jumping out of a CNT was developed in Chapter 3. A similar algorithm was applied in this work. The simulation box was a cube with sides of 100 nm. The CNTs were modeled as cylinders with 0.4nm radius (similar to the CNT radius used in experiments[41]) placed randomly inside the domain and were not connected to each other (Figure 4.2.1). The length over diameter ratio (L/D) of the CNTs was equal to 80 (see Table 4.2.1 for the simulation conditions, and see supplemental material for the justification of using L/D = 80 based on theory[33] and computations[81])

Table 4.2.1. Properties of PS and number of CNTs used in the simulations.

Temperature	Velocity of sound	C_{PS}	ρ_{PS}	D_{PS}
°C	m/s[111]	J/kgK [41]	kg/m³ [112]	x 10^3 cm²/s [113]
-25	2395*	1095	1110*	1.60*
25	2325	1275	1070	1.25
80	2200	1510	1030	1.05

No. of CNTs (wt%, vol%)	470 (5.0%, 4.0%)	830 (10.0%, 8.2%)	2250 (30.0%, 25.7%)

* extrapolated value from references

a)　　　　　　　　　　　　　　　　b)
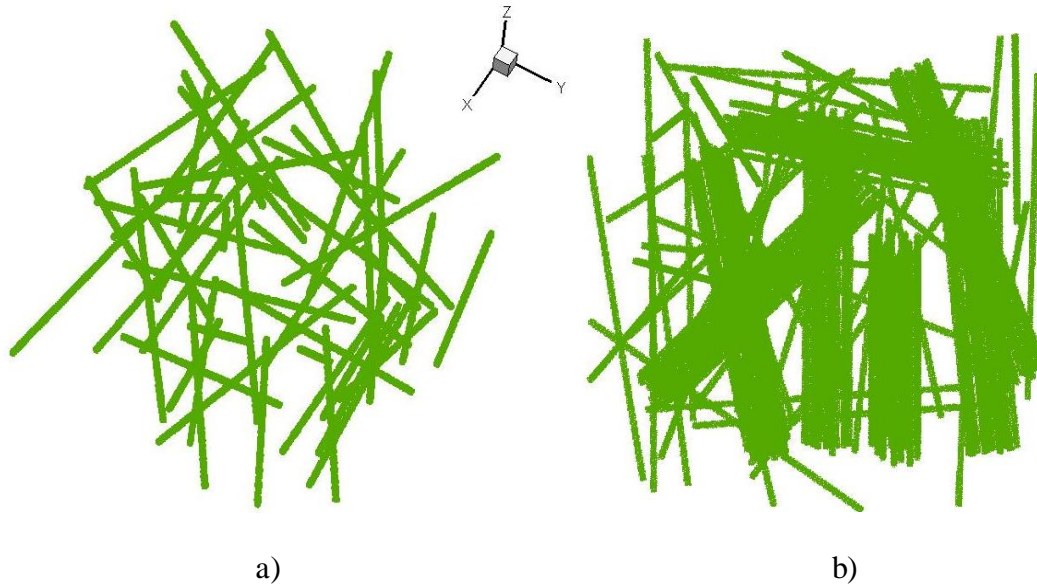
Figure 4.2.1. CNTs randomly placed inside the computational domain as single cylinders at low volume fraction (a) or arranged to form randomly oriented bundles at higher volume fraction (b).

The ratio between the temperature gradients with and without the inclusions (only PS present) provided the ratio of the thermal conductivity of the PS (K_{PS}) divided by K_{eff} for the composite. For each simulated case, 6 runs with different initial geometry

were carried out in order to quantify the uncertainty associated with the random placement of the CNTs (error bars in Figure 4.3.1)

4.3. Results and discussion

The value of f_{m-CN} is an input for the MC simulation. When experimental results are available, f_{m-CNT} can be varied until the computational thermal conductivity becomes equal to that of the experiment, $K_{eff\_exp}/K_{eff\_MC} = 1$. Using this inverse calculation method, we found the values of f_{m_CNT} at different temperatures at 5.0wt% and at 10.0wt% of CNT. According to the acoustic mismatch model (AMM),[6] the relation between f_{m-CN} and the Kapitza resistance, R_{bd}, is $f_{m-CN} = 4 / (\rho_m C_m v_m R_{bd})$, where the subscript m refers to the matrix material in contact with the CNT, ρ is the density, C is the specific heat and v is the velocity of sound (see also Equation (1.2.3)). Our inverse approach leads to the calculation of R_{bd}, which lies between the two extremes found by AMM and the diffuse mismatch model (Table 4.3.1). Furthermore, using the value of R_{bd} calculated based on the Peters et al.[41] data, the K_{eff} found with MC simulations at 0.75wt% and 1.0wt% CNT loadings agree very well with experimental data obtained by another laboratory using the longitudinal steady state heat flow method (Jakubinet et al.[114], see Figure 4.3.1). Based on Table 4.3.1, we obtained the behavior of the Kapitza resistance with temperature: the R_{bd} increased with temperature.

Table 4.3.1. Phonon transmission probability, f_{m_CNT} x10^3, and Kapitza resistance, R_{bd} x10^8(W/m^{2}K)$^{-1}$, calculated from AMM and DMM and from MC simulation. The value of $f_{m\text{-}CNT}$ designated as accepted was used in the MC simulations from now on.

Temp.	$f_{m\text{-}CNT}$ AMM	R_{bd} AMM	R_{bd} DMM	$f_{m\text{-}CNT}$ 5.0wt%	$f_{m\text{-}CNT}$ 10.0wt%	$f_{m\text{-}CNT}$ accepted	R_{bd} accepted
-25 ^{o}C	2.30	59.83	0.04	59.00	65.00	63.00	2.18
25 ^{o}C	2.05	61.65	0.04	56.00	58.00	57.00	2.21
80 ^{o}C	1.69	69.22	0.04	44.00	53.00	47.00	2.48
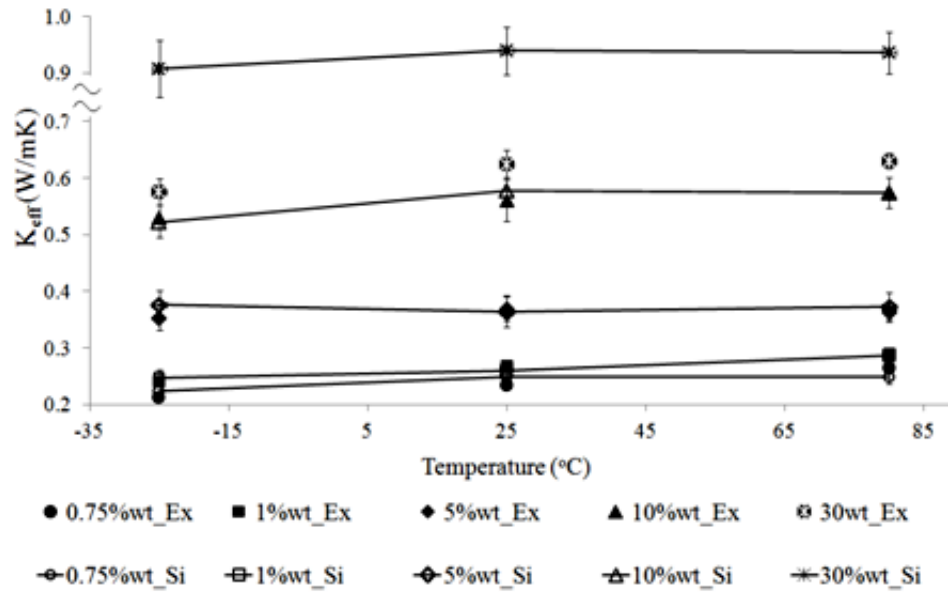
Figure 4.3.1. K_{eff} of CNT - PS composites. The experimental data (points designated as Ex) are from refs.[41, 114]. At each temperature, a single value of Kapitza resistance was used (Table 4.3.1) to simulate the thermal conductivity at various volume fractions (points designated as Si). The error bar was calculated by six different simulations at each point.

However, the question remains: why is K_{eff} of the 30wt% SWNT composite not increasing as much as anticipated? Our simulations for $\leq$ 10.0 wt% CNTs were carried out assuming that only Kapitza resistance at the SWNT-PS interface is important (Figure 4.3.1). Because the simulation results agree with the experimental data and

because the experiments were carried out with care to disperse the CNTs, we can conclude that the R_{bd} at the SWNT-PS interface was the dominant factor and the CNT-CNT resistance had negligible effects up to 10.0wt%. Our simulation attempts to place randomly oriented cylinders inside the simulation box at 30.0wt% CNT (or 25.7% volume) indicated that this is impossible, as expected from Onsager's theory that suggests that random placement of cylinders can be accomplished for vol% inversely proportional to the aspect ratio. However, arranging the cylinders in bundles and in contact with each other at high wt% could be a way to fit 30wt% of CNTs in the domain. Nan *et al.*[33, 34] suggested that K_{eff}, when the CNTs are randomly oriented, is the same as that of parallel CNTs with an angle, θ, relative to the direction of the heat flux such that $\cos^2\theta = 1/3$. Our results indicated that this angle is valid at low vol%, but it changes slightly at higher volume fraction of CNTs. Therefore, we placed the CNTs parallel to each other with an angle to the direction of heat flux. The value of K_{eff} in this case was expected to be the thermal conductivity of SWNT-PS composites at 30.0wt% of CNT loading that included the same R_{bd} as in the case of 0.75wt% to 10.0wt%. As seen in Figure 4.3.1, the K_{eff} obtained from our simulation at 30.0wt% of CNT was about 150% higher than the corresponding experimental data for all temperatures. That means that the CNT-PS resistance is not dominating but, instead, the effect of CNT-CNT resistance must be considerable, to the point of suppressing the K_{eff} of the 30wt% composites.

The CNT-CNT resistance can be calculated based on the results of Duong *et al.*[80], who varied the ratio of the Kapitza resistance of the CNT-CNT interface (R_{bd-C}) relative to that of the CNT-polymer (R_{bd-p}) to obtain values of the ratio of the effective

thermal conductivities in these two cases. Duong *et al.* generated data for different vol% of CNT (see Figure 7 in ref. [80]). Using the ratio of K_{eff} resulting from the present simulations and the value obtained by Peters *et al.*[41] that includes both CNT-PS and CNT-CNT resistance at 25.7vol% CNT, we can find the ratio of $R_{\text{bd-C}}/R_{\text{bd-p}}$ by extrapolation of the data in Duong et al. [41] to 25.7 vol% of CNT. Value of the thermal conductivity of CNT-PS at 30wt% of CNT from experiments is 0.624 W/mK and that of simulation is 0.939 W/mK. The ratio of $K_{\text{eff-contact}}/K_{\text{eff-non-contact}}$ is then equal to 0.664. Based on Figure 7 of in ref. [80]). one can pick different values of the ration $R_{\text{bd-C}}/R_{\text{bd-p}}$ and find the corresponding $K_{\text{eff-contact}}/K_{\text{eff-non-contact}}$ ratio at the same vol% of CNT. The software "Data thief" was used to extract the data more precisely. Following that, a parabolic regression equation is found and used to calculate the value of $K_{\text{eff-contact}}/K_{\text{eff-non-contact}}$ at 25.7 vol% of CNT. The correct value of $R_{\text{bd-C}}/R_{\text{bd-p}}$ ratio will allow $K_{\text{eff-contact}}/K_{\text{eff-non-contact}}$ ratio at 25.7 vol% equal to 0.664 as described above. The value of $R_{\text{bd-p}}$ is taken as 2.21×10^{-8} $W^{-1}m^2K$ for CNT-PS, as seen in Table 3.2.1. The result of this calculation for the CNT-CNT resistance is $R_{\text{bdC-C}} = 12.15 \times 10^{-8}$ $W^{-1}m^2K$. This is higher than 0.11×10^{-8} $W^{-1}m^2K$ obtained from AMM[6], but it is comparable to MD results (Zhong *et al.*[102] reported $8-11 \times 10^{-8}$ $W^{-1}m^2K$ and Maruyama *et al.*[53] found 24.8 $W^{-1}m^2K$, respectively).

Table 4.3.2. Thermal conductivity of CNT-PS composites at 300K with 10.0wt% of CNTs (8.0% vol.). The total number of CNTs is 1000. The CNTs that remained after placing them into bundles were randomly dispersed inside the simulation box, as seen in Figure 4.2.1b.

No. of bundles	50	50	50	25	10	0
No. of CNTs per bundle	15	10	4	15	15	0
K_{eff} , W/mK	0.33	0.38	0.45	0.42	0.54	0.57

In order to examine further the effect of CNT bundling on K_{eff} of high %vol composites, additional MC simulations were carried out at 10.0wt% of CNTs in the PS composite (Table 4.3.2). Kapitza resistance at the CNT-CNT interface was neglected. In the simulations, each bundle of CNTs was generated by first creating a large cylinder having the same length as one CNT and then the CNTs were placed randomly inside this cylinder (see Figure 4.2.1b). As can be seen in Table 4.3.2, both the number and the size of the bundles had a detrimental effect on K_{eff}. This behavior is expected if we consider each bundle that contains several CNTs, as a single cylinder with a smaller aspect ratio than a single CNT.

4.4. Conclusions

In conclusion, Monte Carlo simulations when validated with experimental data can be used to calculate the Kapitza resistance at the CNT-PS interface as well as that at the CNT-CNT interface. Comparison to experiments and inverse calculation of the CNT-CNT resistance provided the value of 12.15×10^{-8} $W^{-1}m^{2}$ K. This is the first time

that the CNT-CNT resistance is found to be higher than the CNT-polymer resistance, based on an interpretation of experimental measurements. Furthermore, the K_{eff} of CNT-based nanocomposites was found to decrease dramatically with the presence of bundles.

Chapter 5: Thermal Behavior of Double Walled Carbon Nanotubes and Evidence of Thermal Rectification[♣]

5.1. Introduction

Recent advances in synthesis and characterization of double-walled carbon nanotubes (DWNTs) suggest that these materials possess enhanced properties compared to those of single-walled carbon nanotubes (SWNTs).[116-119] Kim *et al.*[118] concluded that DWNTs are more thermally stable than SWNTs, as they can withstand temperatures as high as 2000°C without experiencing considerable morphological changes. Koziol *et al.*[119] reported the synthesis of nanotube fibers by directly spinning an aerogel of DWNTs. These fibers were up to three times stronger than commercial Kevlar fibers. Cumings *et al.*[120] characterized multi-walled carbon nanotubes (MWNTs) using TEM and found ultralow-friction and wear-free surfaces in these systems.

In terms of thermal properties, the focus of the present work, the exceptional thermal conductivity of CNTs and GSs[3] has generated promises towards manufacturing nanocomposites with superior thermal management capabilities. Unfortunately, the thermal boundary resistance (TBR, also known as Kapitza resistance)[6, 15] currently hinders such applications. The TBR is the major barrier to heat transfer between the CNTs and the surrounding polymeric matrix.[41, 95, 121, 122] The TBR has been estimated, using molecular dynamics (MD) simulations, for several CNT-polymer and graphene-polymer interfaces (epoxy, polystyrene, PMMA, etc).[77, 79, 95, 97] Values on the order of 10^{-8} Km^{2}W^{-1} have been reported, as seen in

---

[♣] Most of the material presented in this chapter has been published in ref. [115] K. Bui, H. Nguyen, C. Cousin, A. Striolo, and D. V. Papavassiliou, The Journal of Physical Chemistry C 116 (2012) 4449.

Chapter 3 and 4. Functional groups can significantly reduce this resistance.[84, 85, 110, 123] Increasing the thermal transport of nanocomposites by increasing CNT loading has been found not to be applicable in general because of the tendency of nanotubes to form bundles, and because the CNT-CNT TBR is expected to be even higher than that between the CNT and the surrounding matrix (Chapter 5).[53, 102, 107, 124] Yang *et al.*[125] concluded that the CNT-CNT TBR is strongly dependent on contact area. They reported a value of CNT-CNT TBR equal to 1.2×10^{-8} Km^2W^{-1} when two CNTs are aligned and partially overlap each other. On the other hand, this value is ten times smaller, 1.2×10^{-9} Km^2W^{-1}, when two CNTs are crossing each other.

Prior MD simulations have been performed for DWNTs. Rivera *et al.*[126] suggested the possibility of creating nano-sized elements that oscillate along the axial direction at gigahertz frequencies. Zhang *et al.*[127] performed MD simulations of DWNT as rotational bearings and concluded that the interlayer friction coefficient is extremely small, suggesting applications as wear-less bearings. The present work stems from increasing interest focused on DWNTs, with special attention on thermal management opportunities. We seek to determine, via MD simulations, the Kapitza resistance between the two concentric nanotubes forming a DWNT. Our results clarify whether the thermal energy transfer along a DWNT occurs only through the outer CNT, or whether both CNTs contribute to heat transfer. Our results suggest that the TBR between the two nanotubes depends on the direction of heat flux (heat transfer occurs more easily from the outer to the inner CNT than in the opposite direction), suggesting possible applications for DWNTs in thermal rectification in the radial direction.[128, 129]

Thermal rectification properties have been reported for systems with defects in their structure or when impurities are present. Wu *et al.*[130] reported thermal rectification at intramoecular junctions formed by introducing pentagon-heptagon rings in SWCNTs. Chang *et al.*[131] concluded that as carbon and boron nitride nanotubes were mass-loaded with heavy molecules, the resulting nanoscale system yielded asymmetric axial thermal conductance with greater heat flow in the direction of decreasing mass density. Graphene ribbons also possess thermal rectification properties when their structure is asymmetric.[132] Through this work, we find that thermal rectification properties can be achieved in the radial direction for a pure, symmetric (around its longitudinal axis), and defect-free DWNT.

5.2. Simulation setup

5.2.1. Freestanding DWNTs

DWNTs in vacuum were generated with different lengths, ranging from 2.8nm to 30nm. The chirality of the two nanotubes in a DWNT was either the same [i.e., a (5,5) SWNT inside a (10,10) SWNT, indicated as (5,5)-(10,10) DWNT], or different [i.e., (6,6)-(19,0) DWNT and (5,5)-(16,5) DWNT]. In all cases the inter-tube distance was 0.34nm. See Figure 5.2.1 for a simulation snapshot. MD simulations were performed using the package LAMMPS.[43] The Tersoff potential[44] was employed to describe the interaction among carbon atoms within one nanotube. The interaction between carbon atoms of different nanotubes was described using the 12-6 Lennard-Jones (LJ) potential (see Equation (2.1.2)).

a)	b)
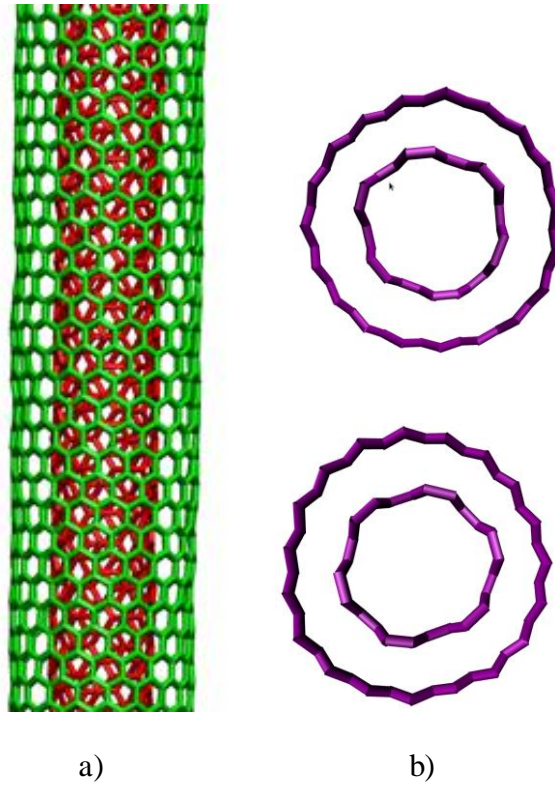
Figure 5.2.1. The DWNT is composed of one armchair (6,6) SWNT inside a zigzag (19,0) CNT. The figure represents the lateral view of one section of the DWNT collected during the relaxation stage (a) and two cross-sections obtained at the midpoint of the DWNT (b). The two cross sections are obtained at a 1ps interval to illustrate how the SWNTs deform, relative to their original cylindrical shape, as the simulation progresses.

Details about the models and the parameters used and about the implemented protocol have been described elsewhere (see Appendix A).[49, 110, 121, 133] The methodology is based on non-equilibrium MD simulations as described in Chapter 2. The DWNT in vacuum was heated from 50 K to 300K, and then equilibrated at 300 K for 600 picoseconds (NVT ensemble). For the next 200 picoseconds, the system relaxed under the NVE ensemble in order to record 15 different and independent configurations. Each of the 15 configurations was used to initiate non-equilibrium simulations used to extract the thermal boundary resistance. One of the two SWNTs within the DWNT was

instantaneously heated to 500 K ('hot' SWNT). The hot SWNT was maintained at 500K for 10 picoseconds to relax the newly excited vibration modes (NVT ensemble), while the other SWNT was maintained rigid. Then the simulation progressed in the NVE ensemble with one SWNT at initial T of 500K, and the other at 300K. During the latter NVE portion of the simulation, heat flowed from the hot SWNT to the cold one. The temperature difference between the two SWNTs was recorded as a function of time and fitted to Equation (2.1.3) to obtain the relaxation constant, τ. The Kapitza resistance, R_{bd}, is obtained from τ via Equation (2.1.4), based on the lumped capacitance model. [50, 51, 121, 123] To obtain heat capacity of each nanotube, C_T, each corresponding nanotube was isolated and simulated within the NVT ensemble at 300, 400 or 500 K for 400ps (Equation (2.1.5)).

The lumped capacitance model is expected to hold when the temperature of the surrounding system does not change significantly during the NVE stage of the simulation. Although in the system simulated here the temperature of the cold SWNT changes with time, it is necessary to assess the validity of the underlying assumptions. The Biot number for this system, defined as $Bi=hL/k$, where h is thermal conductance (equal to inverse of the Kapitza resistance in this case), L is the distance through which heat is transferred and k is the thermal conductivity of the SWNT, can be used to define a criterion for the applicability of the lumped capacitance model.[51] When $Bi < 0.1$, then the lumped capacitance model can be used, and Equation (2.1.4) is expected to yield reliable estimates for the Kapitza resistance.[51] In our case, assuming a typical value of k = 2900 W/(mK), L =0.34nm and h = 0.1 x 10^8 W/(m^{2}K), the Biot number is found to be 1.17 x 10^{-4}, well below the value of 0.1.

The procedure of creating an amorphous silica coating is described as follows: first, a 10nm (5,5)-(10,10) DWNT was inserted at the center of a 5x5x15nm^3 block of crystalline silica (cristobalite). Next the silica was slowly heated to 6000K and kept at that temperature for 20ps under NVT ensemble. Finally, the system was slowly cooled down to 300K. Both the heating and cooling rate are 10^{12} Ks^{-1}, which is similar to the procedure described by Ong *et al*.[57]. Note that the DWNT was frozen during this process but there exists the Lennard Jones potential between the outer nanotube and the silica. By initially inserting the nanotube to the crystalline silica before the melting step, we can obtain a better coating than just simply placing the DWNT inside the amorphous silica (see Figure 5.2.2).
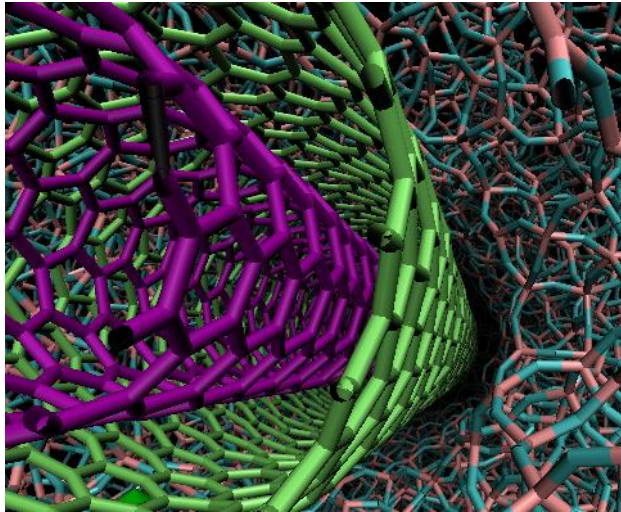
Figure 5.2.2. Snapshot of the amorphous silica coating that coats a DWNT during NVE simulations**.**

In order to calculate simultaneously the Kaptiza resistance between two nanotubes as well as between the outer nanotube and the coating, Equation (2.1.4) is no longer applicable. This is because the lumped capacitance model, where Equation

(2.1.4) was derived, consists of only two components: the hot/cold object and the environment. For this system of interest, there are three components (the silica coating, inner and outer nanotube) that contribute to thermal transfer. Instead, the Green-Kubo method was used to calculate the Kapitza resistance in this system. As discussed in section 2.1.4, this method is an equilibrium approach to calculate the heat flow across the interface over time (NVE ensemble).

5.3.   Results and discussions

5.3.1. Effect of nanotube length and chirality on Kapitza resistance

Shenogin et al.[121] investigated the Kapitza resistance of a CNT-octane system and found that the Kapitza resistance changes as a function of the CNT length. The results converged when the nanotube length approached 8.6 nm. The reason for this length dependence is the availability of more long-wavelength phonons for heat transfer as the tube length increases. Our results show that the Kapitza resistance between inner and outer nanotube increases as the length of the nanotube increases from 2.8nm to 20.0nm, but then it reaches a plateau when the DWNT length is in the range of 20.0nm to 30.0nm (see Figure 5.3.1). Unlike the CNT-octane case, in which the soft phonons with frequencies less than 5 THz govern heat transfer, high frequency optical phonons in the range 60-65 THz appear to govern the heat transfer for the CNT-CNT system considered here (see Figure 5.3.2). Our results are consistent with results from Shiomi et al.,[38] who studied the heat conduction in a single-walled CNT using the heat pulse technique. They reported that at non-equilibrium condition, most of the energy is

distributed to the bands higher than 50 THz, corresponding to optical phonons. These can play a major role in heat transfer.
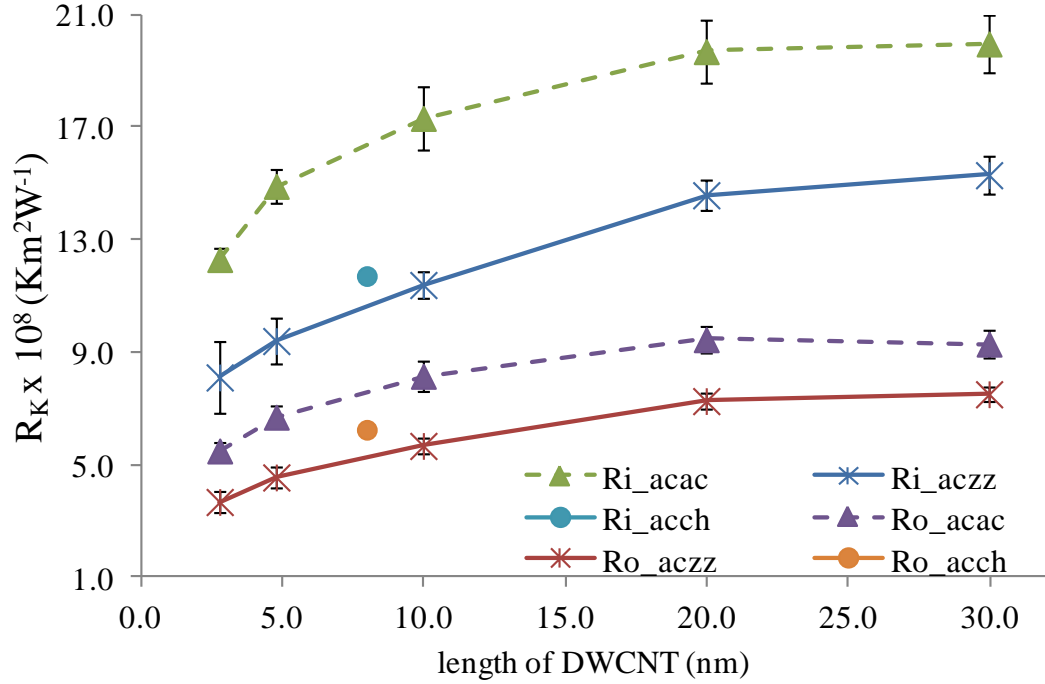
Figure 5.3.1. Kapitza resistance between the two SWNTs composing DWNTs of different lengths and chiralities. The notations "i" and "o" indicate that either the inner or the outer nanotube was heated, respectively. The notations "acac", "aczz" and "acch" indicate (5,5)-(10,10), (6,6)-(19,0) and (6,6)-(16,5) DWNTs, respectively. The error bars were calculated from 15 simulations with different initial configurations with Student t-test (95% level of confidence).

Because of the structural similarities, one could expect that the Kapitza resistance is less when both SWNTs composing one DWNT have the same chirality. Our results (see Figure 5.3.1) indicate the contrary. The Kapitza resistance is smaller for the armchair-zigzag DWNTs, and larger for armchair-armchair systems. Results for the DWNT composed by one (6,6) SWNT in a (16,5) SWNT lie in between the other two cases. To explain this finding, the Fourier transform of the velocity autocorrelation

function for carbon atoms is plotted in Figure 5.3.2. The frequencies at which maxima and minima of the vibration spectrum occur for the interior (6,6) SWNT match the frequencies of maxima and minima of the vibration spectrum of the (19,0) SWNT in a (6,6)-(19,0) DWNT. In comparison, the frequencies at the maxima and minima of the spectrum of the (5,5) SWNT do not match as well the maxima and minima of the (10,10) SWNT in a (5,5)-(10,10) DWNT. This implies that heat can transfer more easily between an armchair and a zigzag nanotube than in the other case. We also calculated the Kapitza resistance of a (6,6)-(16,5) DWNT of length 7.8nm, and the result lies in between those obtained for armchair-armchair and armchair-zigzag DWNTs (see Figure 5.3.1).

a)   b)
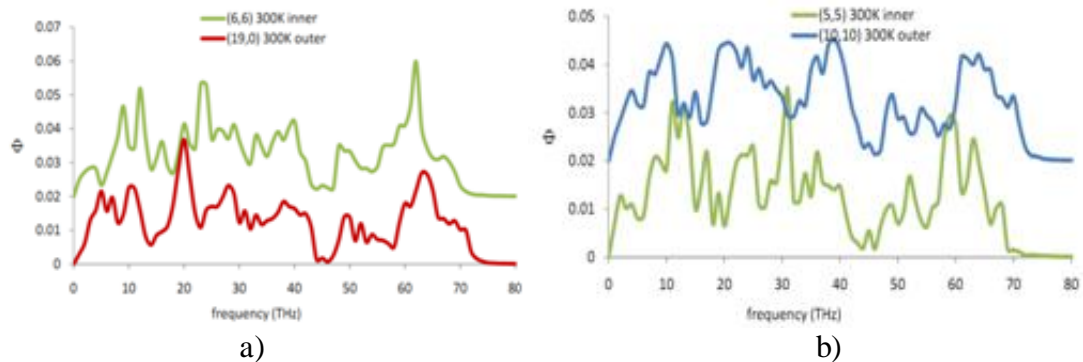
Figure 5.3.2. Fourier transform of the velocity autocorrelation function for carbon atoms in (6,6)-(19,0) (a) and (5,5)-(10,10) DWNTs (b). Both DWNTs are of length 4.8nm.
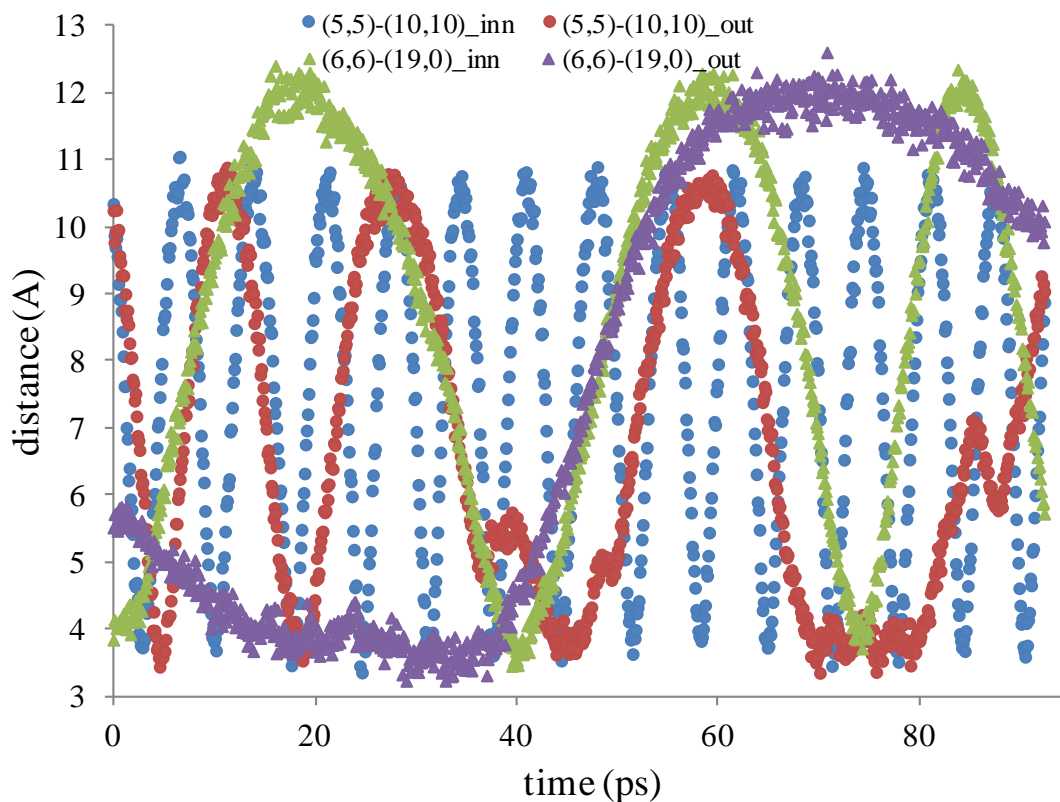
Figure 5.3.3. Distance between 2 neighbor carbon atoms belonging to inner and outer nanotubes in a DWNT during heat transfer. The notations "inn" and "out" indicate the nanotube that is heated. The length of the DWNTs is 4.8nm. The periodicity observed in the data corresponds to the periodicity of the relative rotation of the nanotubes composing the DWNT.

Visual analysis of our simulation results (sequences of snapshots such as those in Figure 5.2.1) showed that the two nanotubes in a DWNT can rotate relative to each other – a behavior explored by others with focus on wear-less bearings.[127] For the scope of this work, it is worth to point out that when the inner SWNT is heated the rotational period for the DWNTs is about 7 ps for the armchair-armchair DWNT, and 40 ps for the armchair-zigzag DWNT (see Figure 5.3.3). Considering the period of

rotation obtained from Figure 5.3.3 and the Kapitza resistance of the corresponding DWNTs, we observe that higher rotation speeds lead to higher resistances to heat transfer, probably because of weaker coupling between the mechanical vibrations of the carbon atoms belonging to the two interacting nanotubes. Based on this observation it is likely that those DWNTs that provide poorer thermal transport properties will be those more suitable for the production of wear-less bearings.

Our estimates for the Kapitza resistance within concentric DWNTs are consistent with estimates reported by others for that between CNTs touching via their external wall.[53, 77, 95, 102, 110, 121] More importantly, the values of the Kapitza resistance obtained in all cases considered in this work are always larger than those typically observed at the CNT-polymer interface (e.g., 2.61×10^{-8} Km^2W^{-1} for CNT-epoxy[78], 0.95×10^{-8} Km^2W^{-1} for CNT-PMMA[81], 2.21×10^{-8} $Km^2W^{-1}$for CNT-polystyrene[107]). Our results, thus, suggest that when DWNTs are used in thermally-conductive composites the heat is likely to transfer mainly through the outer SWNT, while the inner SWNT does not contribute to thermal management. (Note also that values of the Kapitza resistance in other solid-solid interfaces are smaller than the CNT-CNT resistances calculated herein, e.g., 0.12×10^{-8} Km^2W^{-1} for GaN/SiC, and 0.1×10^{-8} Km^2W^{-1} for GaN/Sapphire[134, 135].)

5.3.2. *Evidence of thermal rectification*

Another important observation can be obtained from the results shown in Figure 5.3.1. Specifically, given one DWNT, the Kapitza resistance estimated when the outer SWNT is heated is lower than that obtained when the inner SWNT is heated. This suggests that the heat flux preferably travels from the outer to the inner SWNT than

vice versa. This behavior is explained by mechanical observations. When a SWNT is heated, it expands in the radial direction, and vice versa, when it is cooled it contracts. When heat transfers from the outer to the inner SWNT within a DWNT, the inner SWNT expands upon heating, while the outer SWNT contracts upon cooling, improving mechanical coupling between the two nanotubes. On the other hand, when heat transfers from the inner to the outer SWNT the mechanical expansion/contraction leads to less mechanical coupling as the heat-transfer process progresses. This different behavior is quantified in Figure 5.3.4, in which the average distance between the two concentric SWNTs is shown when heat transfers from the outer to the inner, or from the inner to the outer. The average distance between the two SWNTs decreases in the former case, and increases in the latter. A small change in the tube-tube distance causes strong effects on the dispersion forces between the two nanotubes, thus affecting the Kapitza resistance.
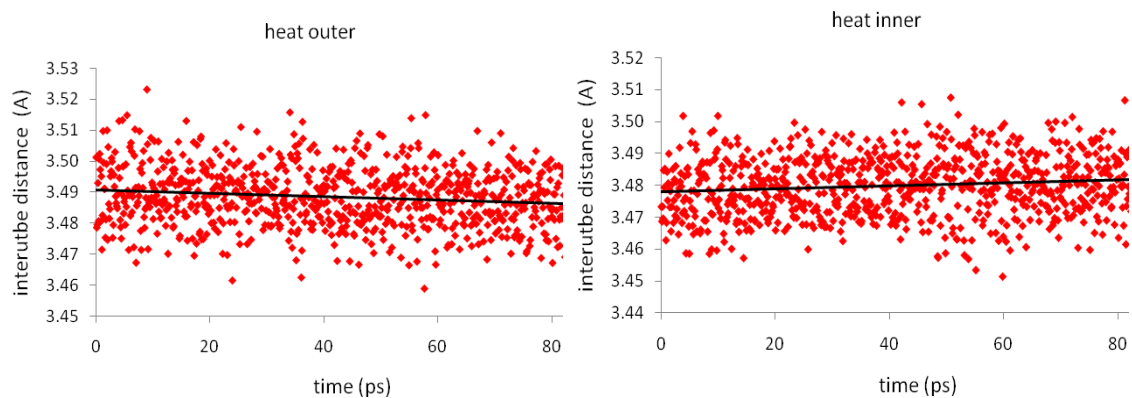
Figure 5.3.4. Average distance between two SWNTs decreases during the relaxation step as the outer or inner one is heated for (5,5)-(10,10) DWNT, as seen on the left panel. On the contrary, this average distance increases when the inner nanotube is heated due to the expansion/contraction behavior, as seen on the right pannel. Similar tendency is also observed for other DWNTs.

In order to assess whether the difference in Kapitza resistance observed when heat transfers from the inner to the outer SWNT in DWNTs is sufficient to provide thermal rectification in the radial direction, we calculate the thermal rectification factor, R_{REC}, defined as

$$R_{REC} = \frac{K_+ - K_-}{K_-} \times 100\%$$

(5.3.1)

In the above equation, K_+ is the thermal conductance (i.e., the inverse of the Kapitza resistance) as heat transfers from the outer to the inner SWNT and K_- is thermal conductance in the opposite direction.

Table 5.3.1. Thermal rectification factor in the radial direction, R_{REC}, for (6,6)-(19,0) and (5,5)-(10,10) DWNTs of different lengths.

Length (nm)	2.8	4.8	10.0	20.0	30.0
(6,6)-(19,0) DWNT	120.1%	106.3%	100.7%	100.6%	103.6%
(5,5)-(10,10) DWNT	123.6%	122.4%	112.4%	108.3%	114.7%

As can be seen from Table 5.3.1, R_{REC} is lightly smaller for the (6,6)-(19,0) compared to the (5,5)-(10,10) DWNT. As the DWNT length increases from 2.8 and 4.8nm, R_{REC} decreases about 20%. It reaches a plateau for longer DWNTs. This trend is similar to the one reported by Yang *et al.*[132] for asymmetric graphene ribbons. The rectification ratio was as high as 240% for short ribbons. As the length of the ribbons increased from 3.4 to 5.1nm, this ratio decreased from 240% to 92% and remained constant for longer ribbons. Those authors reported that, for asymmetric graphene ribbons, the graded geometric asymmetry is the key for the increase of the rectification ratio. On the other hand, evidence of thermal rectification in DWNTs is attributed here

to the expansion/contraction behavior of individual CNTs. Interestingly, our results suggest that symmetric (around their longitudinal axis) and defect-free DWNTs exhibit a R_{REC} in the range of 103%-114% for DWNTs of length exceeding 10nm.

5.3.3. *Kapitza resistance between nanotube and silica*

As we can see in Figure 5.3.5, the Kapitza resistance between the outer nanotube and the silica coating (R_cs) is significantly smaller than that between the inner and outer nanotube (R_cc). This is a confirmation that, whether the DWNT is embedded or free standing, thermal transfer is expected to take place mainly at the outer nanotube. When increasing the nanotube length from 10 to 20nm, R_cc keeps increasing, while R_cs remains constant. This is due to the lack of long-wavelength phonons in size-limited nanotube (ballistic properties) that contribute to heat transfer between the inner tube and the outer one. For the case of amorphous silica, in which the phonon mean free path is a lot shorter, all of the available phonons are excited and contribute to heat transfer. Note that values of R_cc in Figure 5.3.5 are slightly smaller than those in Figure 5.3.1. As pointed out by Hu *et al*.[136], values of Kapitza resistance obtained from transient method (thermal relaxation) are several times larger than those calculated by the direct simulation method of heat flow across the interface.
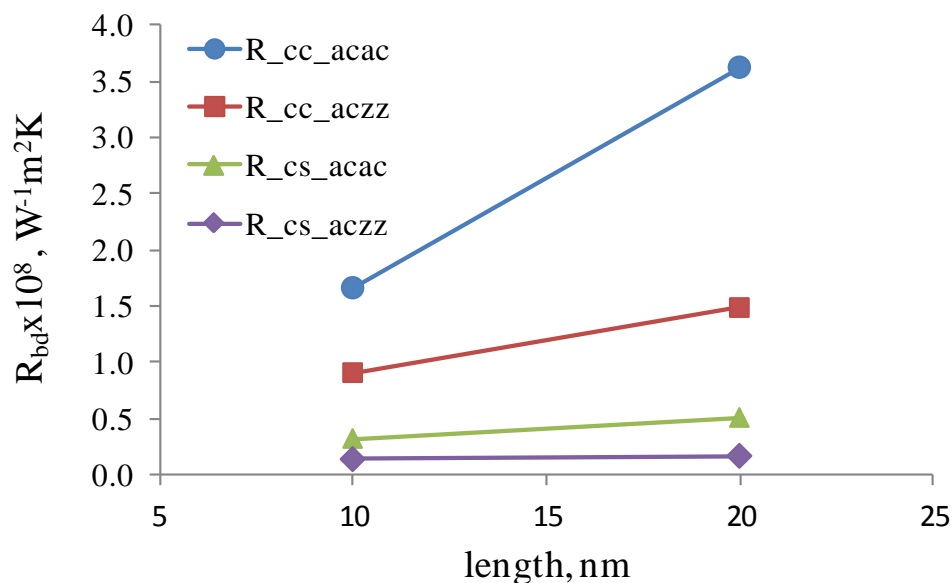
Figure 5.3.5. Kaptiza resistance between the inner and outer nanotube (R_cc) , and between the outer nanotube and silica (R_cs) at different length of the nanotube. The DWNT can be either (5,5)-(10,10), noted as acac, or (6,6)-(19,0), noted as aczz.

5.4. Conclusions

To summarize, we employed both non-equilibrium and equilibrium molecular dynamics simulations to estimate the resistance to heat transfer (known as thermal boundary resistance or Kapitza resistance) between two concentric single walled carbon nanotubes forming a double walled carbon nanotube (DWNT), and between the outer nanotube and amorphous silica. We confirmed that, whether the DWNT is embedded or free standing, thermal transfer is expected to take place mainly at the outer nanotube.

The calculations were performed for DWNTs of increasing length, and it was found that high frequency optical phonons in the range 60-65 THz govern heat transfer in the system considered here, unlike soft phonons of frequency less than 5 THz that were found to govern heat transfer between carbon nanotubes and octane. In agreement with results obtained for carbon nanotubes in configurations other than the one

considered here, our results show that the resistance to heat transfer between the concentric nanotubes is larger than that between carbon nanotubes and organic matrixes, suggesting that when DWNTs are used in thermally-conducting nanocomposites heat travels predominantly along the outer nanotube, while the inner nanotube does not contribute to thermal management. DWNTs of different chirality were considered, and it was found that the Kapitza resistance is smaller in armchair-zigzag DWNTs than in armchair-armchair DWNTs. By examining the relative rotation of the two nanotubes, it was found that those carbon nanotubes that seem to have frictionless movement (faster rotation) are characterized by higher thermal boundary resistance, suggesting that mechanically coupling the vibrations of carbon atoms in the two concentric carbon nanotubes facilitates heat transfer. Comparing the thermal boundary resistance for DWNTs in which either the outer or the inner carbon nanotube was heated, it was found that, because of better mechanical coupling, heat transfer occurs much more easily from a hot outer carbon nanotube to a cold inner one than vice versa, yielding thermal rectification factors in the radial direction in the range 103-114 % for longitudinal symmetric, defect-free DWNTs of length exceeding 10 nm. Even though a temperature difference of about 200K between two walls might not be practical, these results help understand heat transfer in carbon nanotubes, and they might be useful for opening up new opportunities for applications of double walled carbon nanotubes in thermal rectification applications.

Chapter 6: Numerical Calculation of the Effective Thermal Conductivity of Nanocomposites

6.1. Introduction

The discovery of thermal boundary resistance (TBR) at the metal-liquid helium interface by Kapitza [15] has laid the foundation for extensive research in the field of interfacial heat transfer. Recently, the interest of scientists in this phenomenon has been re-invigorated due to the emergence of carbon based nanomaterials, such as carbon nanotubes (CNTs) and graphene sheet nanoribbons (GSs) [41, 56, 78, 106, 114, 137, 138]. Because of the outstanding properties of these nanomaterials, there have been quite high expectations to manufacture composites and fibers with also exceptional properties [3, 84, 119, 122, 139]. Nevertheless, due to the extremely high surface area of CNTs and GSs, TBR at the interface between the nanoinclusions and the polymer matrix plays a dominant role that suppresses the effective thermal conductivity (K_{eff}) of composites [35, 41]. There have been numerous papers using either experiments or simulations to characterize/measure TBR and to suggest ways to improve heat transfer in nanocompsites [49, 50, 53, 80, 84, 124, 140].

For the purposes of designing/producing composites with superior thermal management capabilities, it is essential to accurately predict K_{eff}. This is not a trivial task, because of the not so well-known physical properties (i.e., TBR between CNT-polymer and TBR between CNT-CNT, ballistic heat transport [14, 38]) and the uncertain configurations and dispersion state of CNTs or GSs in the polymer matrix. Analytical formulas derived from effective medium approximation (EMA) [33, 34] can be used to estimate K_{eff} for CNT-based nanocomposites assuming that all CNTs are

straight cylinders and parallel to each other. Kumar *et al.* [35, 36] developed a computational model for thermal and electrical transport by explicitly generating a random network of straight cylinders representing CNTs in 2D. Their approach employed a finite volume discretization scheme to calculate the temperature distribution and K_{eff} for CNT-based nanocomposites. However, results from both this approach and EMA did not agree with experimental data at high volume faction of CNTs in composites, because the TBR between neighbouring CNTs in contact is another crucial factor suppressing K_{eff} [53, 107, 141, 142]. Furthermore, the configuration of CNTs and GSs in polymer matrix is not such that they are perfectly straight and uniformly dispersed. Instead, they can be twisted and bended into worm-like geometries and/or stacked together into bundles [41, 65, 66].

The persistence length (L_p) is a commonly used parameter to quantify the flexibility of a chain [71]. The dynamic bending persistence length refers to bending behavior due to the thermal energy and the stiffness of a filament. On the other hand, the static bending persistence length is used when bending points are due to structural defects. When the contour length (L) of a CNT is larger than its L_p, the tube is usually under significant bending. In the absence of flow, single-walled CNTs behave like rigid rods (when $L << L_p$) or as semiflexible rods (when $L \approx L_p$). Measurements of L_p obtained for single-walled CNTs by real-time visualization have indicated values between 32 and 174 μm [70, 143]. Lee *et al.* [66, 75] reported the value of L_p for multi-walled CNTs to be 271 nm due to static bending, which is significantly smaller than the dynamic persistence length.

Recent work of Duong *et al.* [79] and Bui *et al.* [107] has reported that K_{eff} could be reduced by up to 40% when CNTs are placed in bundles, instead of being well-dispersed in the polymer matrix. To our knowledge, no prior work has investigated simultaneously both the effect of TBR and CNT persistence length on K_{eff}. One possible reason is because of the complexity of generating realistic configurations of CNTs that mimic those under experimental conditions. Molecular dynamics (MD) simulations are capable of investigating TBR at the atomic scale. This approach is inefficient for the study of K_{eff} for large systems, since the number of carbon atoms in CNTs in addition to those in the polymer molecules is in the millions [84]. In our previous work [77, 80, 107, 133], an off-lattice Monte Carlo simulation technique has been developed and used to study heat transfer in CNT-based and GS-based nanocomposites for simple cases, where the inclusions are perfectly straight and well-dispersed. The purpose of the present work is to present an algorithm that is capable of generating rather realistic configurations of CNTs by incorporating the persistence length of CNTs in the polymer matrix. Following that, we employ off-lattice Monte Carlo (MC) techniques to study heat transfer in nanocomposites by taking into account simultaneously both the effect of TBR and the configuration of the CNTs. Finally, our results are validated with experiments for MWNT/epoxy systems and provide guidance to practically improve K_{eff}.

6.2. Methodology

6.2.1. Algorithm for generating CNTs with worm-like geometry

Each CNT is composed of the same number of segments, noted as *N*. Each of these segments is a straight solid cylinder. The length of each cylinder is noted as *Δs*

and its radius is noted as R. The contour length of a CNT, noted as L, is equal to the segment length multiplied by the number of segments, while the end-to-end length of a CNT is noted as L_e. The procedure of generating worm-like CNTs has been described in section 2.2.1 of Chapter 2. By varying the critical angles between each segment, $\phi_{critical}$ and $\varphi_{critical}$, one can generate CNTs with different degrees of bending/twisting or, in order words, different values of L_p (Figure 2.2.1). For each simulation, mean and variance of L_p are computed in order to control the geometry of CNTs. As a result, the pre-processing step of generating the configuration of CNTs inside the computational box is completed. The configuration of CNTs in this work is similar to those SEM images reported by Lee *et al*. [66, 75] (see Figure 2.2.2). The next step is the simulation of heat transfer by means of Monte Carlo simulations.

6.2.2. *Monte Carlo simulations*

Details of Monte Carlo simulations has been described in section 2.2.2 of Chapter 2 for simple geometries. Note that the geometry of each worm-like CNT is different from the others due to the random relative angles between each segment. The MC simulations require an effective algorithm to distribute heat walkers randomly inside the current CNT or to place them close to the surface before jumping out of that CNT. This was done by developing a small program that extracted those grid cells that belong to the outer surface of each CNT and creating a shell that represents the outer surface of each CNT (Figure 6.2.1).

As a result, a heat walker can be randomly placed inside a CNT by first picking an arbitrary grid cell belonging to that CNT, i.e., grid cell i with its centre located at (x_i, y_i, z_i). Second, the heat walker is placed randomly within that grid cell. Similarly, a heat

walker can be placed randomly within a shell close to the surface of a CNT by picking an arbitrary grid cell belonging to those of the outer surface of that CNT (Figure 6.2.1b). Because the size of the simulation box affects computational cost, there needs to be a balance between the resolution of the system and the computational cost. Our results suggest that the ratio of one unit length in simulation over 1nm in real scale is 3:1 in order to model the CNTs effectively.

a)   b)
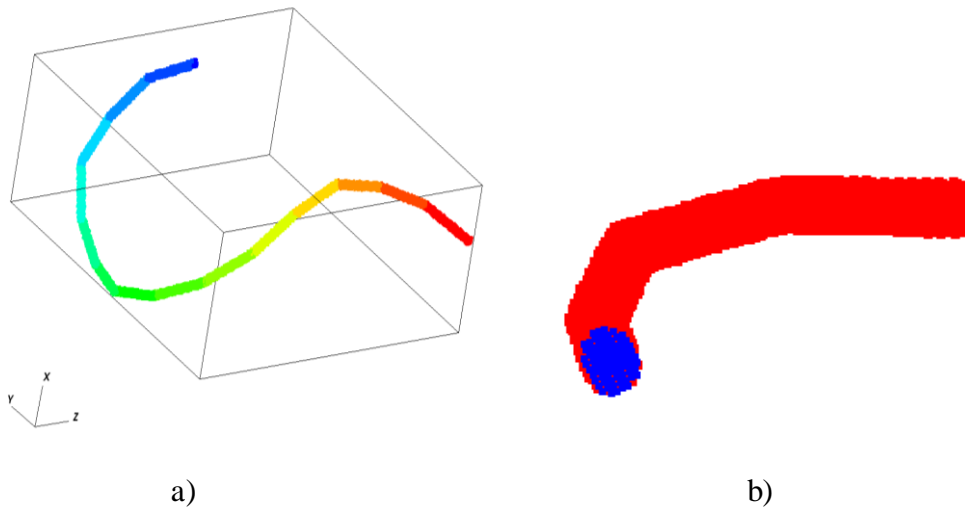
Figure 6.2.1. a) One worm-like CNT (contour length of 450nm, end-to-end length of 180nm, persistence length of 100nm) consisting of 15 segments (in different colors) is generated inside a computation box of 450x200x200 grid. b) A slice through the CNT revealing 2 distinct regions: those grid cells belonging to the shell that forms the outer surface of the CNT are marked in red while the remaining grid cells are in blue color.

6.2.3. Estimation of persistence length from TEM images and validation with

experiments

Base on TEM images of MWNTs reported by Guo *et al*.[144], we can extract the position of each segment belonging to one nanotube and estimate L_p of that nanotube (see Equation (2.2.3)). This procedure is similar to those reported by Gittes *et*

al.[71] and Fakhri *et al.*[65]. These MWNTs, having the same L_p as those from experiments and $L = 450$nm, were generated inside the computational box for validation purposes. The size of the box is 450x300x300 mesh points, in which the longest dimension is the also the direction of heat flux (x-direction). In our simulations, periodic boundary conditions are applied in three directions and those tubes outside of the box are rolled back. Note that the MWNTs can be broken and possess unequal length under experimental conditions. In this work, the CNTs will be broken into new ones if they intercept the boundary in the x-direction as in Figure 6.2.3b. This scenario provides better replication of experimental conditions since individual CNTs will not possess exactly the same configuration in reality.
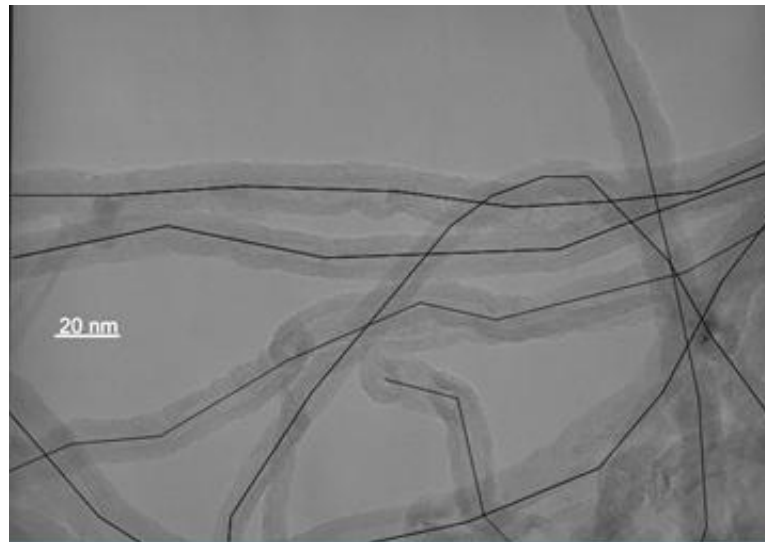
Figure 6.2.2. TEM images of pristine MWNTs taken by Guo *et al.*[144]. The straight segments were drawn along the center of each nanotube. Position of these segments were recorded to calculate the persistence length (L_p).

a)   b)
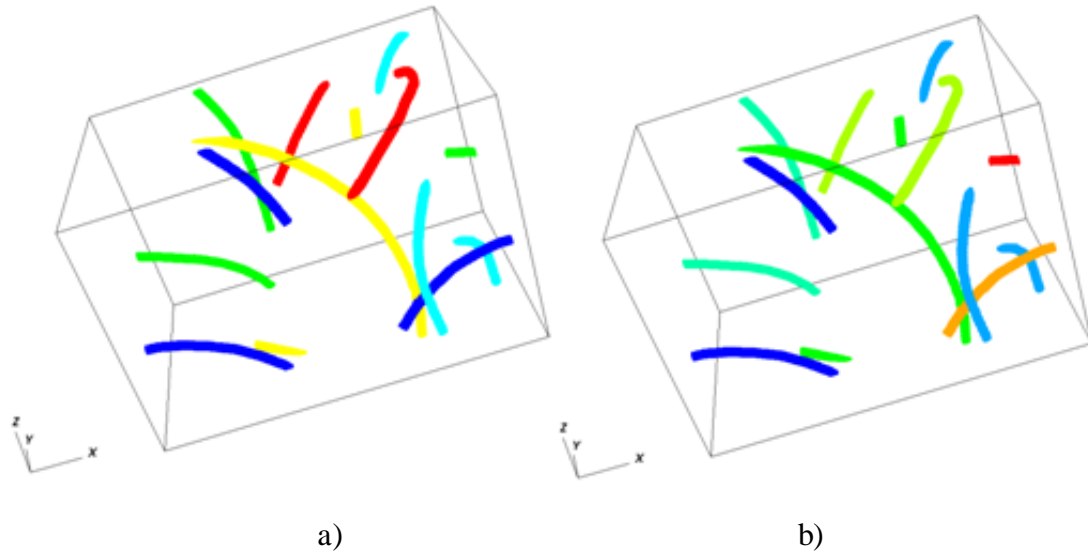
Figure 6.2.3. Five worm-like CNTs that were generated randomly inside the computational box. Different colors were used to distinguish different tubes. Periodic boundary condition was applied in 3 directions. a) Those segments of the tubes that are outside were rolled back through the other side of the box. b) Those segments of the tubes that intercepts with the boundary in x-direction, the direction of heat flux, were considered as different CNTs as they were rolled back into the box.

6.3.   Results and discussions

6.3.1. Equilibrium simulations

Equilibrium simulations were performed to determine the shape factor, C_f, which is described in Equation (2.2.2). As we can see in Figure 6.3.1, the value of the shape factor for one CNT was found to be 0.39. This value was double checked in another simulation, in which there were 5 CNTs placed inside the computation box. Because the orientation and placement of CNTs were random, the vol.% of each CNT was slightly different from each other (Table 6.3.1). By calculating the heat walker density inside each CNT during equilibrium simulations, we can see that these values were fluctuating around the vol.% of each CNT. This serves as comfirmation that $C_f=$ 0.39 is the correct shape factor for the worm-like CNTs.

85
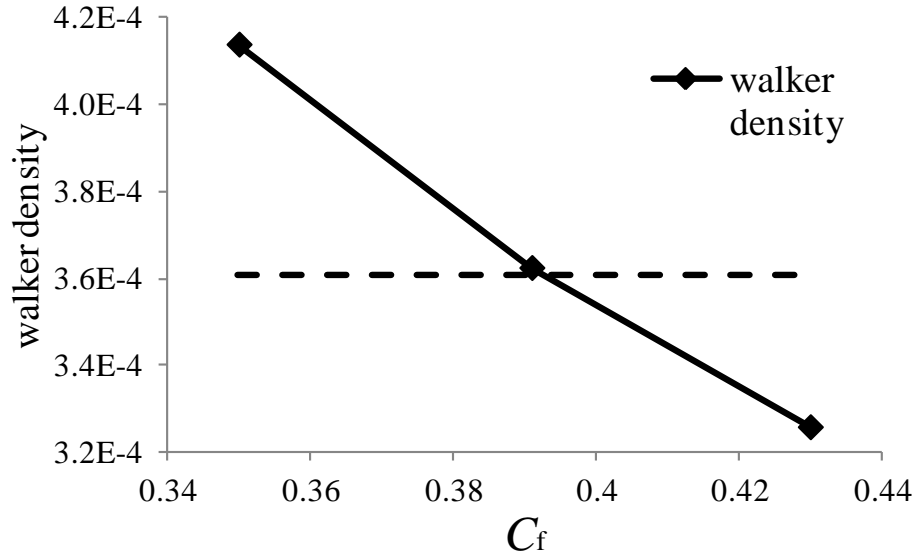
Figure 6.3.1. Heat walker density inside a CNT versus equilibrium shape factor, C_f, during equilibrium simulations. The correct value of $C_f = 0.39$ will result in an equal value between walker density inside a CNT and the vol% of that CNT in the computation box**.**

Table 6.3.1. Heat walker density of 5 CNTs inside a computational box during equilibrium. Because the heat walker density inside each CNT fluctuates around the vol% of corresponding CNT, it is confirmed that $C_f = 0.39$ is a correct choice for the equilibrium shape factor.

	CNT index	1	2	3	4	5
	CNT vol%	3.72E-04	3.61E-04	3.64E-04	3.59E-04	3.62E-04
% of	$t=1000\Delta t$	3.70E-04	3.60E-04	3.68E-04	3.69E-04	3.62E-04
walkers	$t=1500\Delta t$	3.70E-04	3.60E-04	3.68E-04	3.53E-04	3.61E-04
inside	$t=2000\Delta t$	3.77E-04	3.71E-04	3.61E-04	3.65E-04	3.63E-04
the CNTs	$t=2500\Delta t$	3.68E-04	3.56E-04	3.58E-04	3.66E-04	3.65E-04

The distribution of heat walkers along the *x*-direction (also the direction of heat flux) for every 100,000 time steps during isoflux simulations is plotted in Figure 6.3.2. When the number of time steps is equal to or higher than 900,000, the slope is stable indicating that steady state has been reached. The effect of the number of heat walkers released in every time step on the results during isoflux simulations was also studied and plotted in Figure 6.3.3. When the number of heat walkers is equal or higher than 90,000, stable results are obtained. Because of computational cost, we chose the number of time steps and number of heat walkers to be 900,000 and 90,000 respectively, which are large enough to obtain converged results.
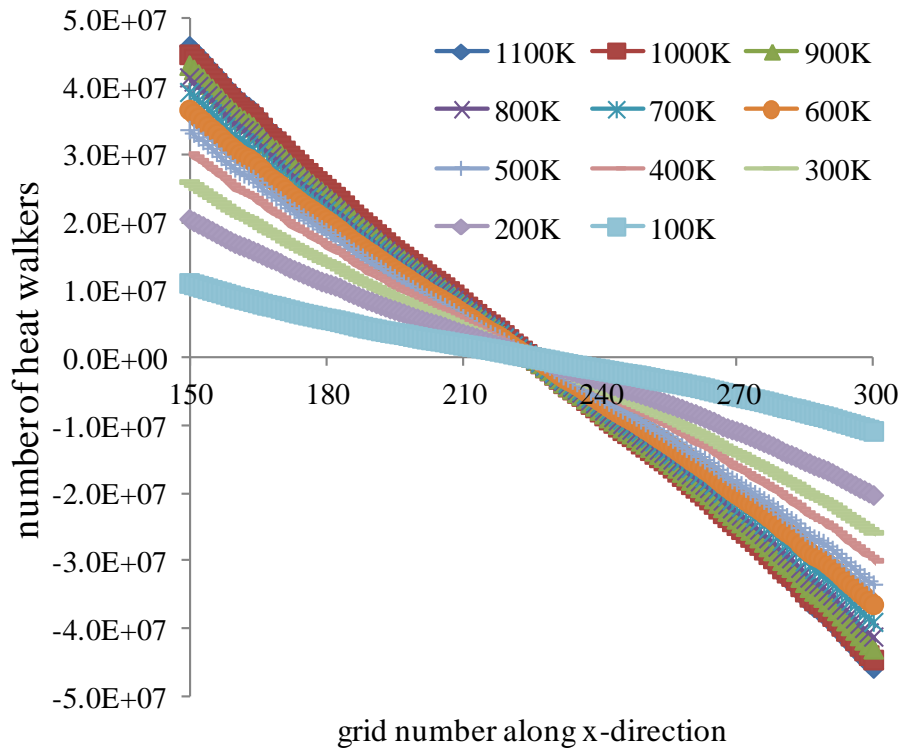
Figure 6.3.2. Distribution of heat walkers along the *x*-direction (i.e., the direction of the heat flux) for every 100,000 time steps during isoflux simulations. The inverse of the slope these lines is proportional to the thermal conductivity of the system. When the number of time steps is equal to or higher than 900,000, the slope is stable indicating the steady state.
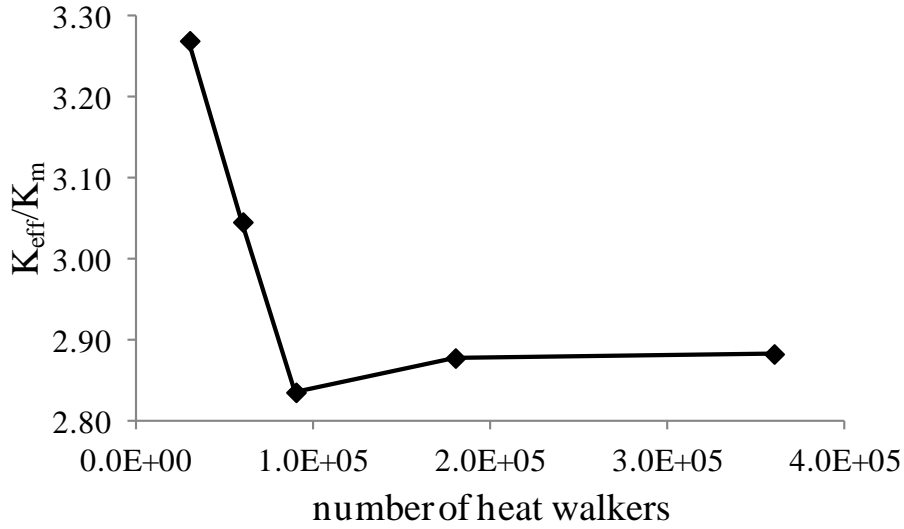
Figure 6.3.3. Effect of number of heat walkers released every time step on the results during isoflux simulations. When the number of heat walkers is equal or higher than 90,000, stable results is obtained.

6.3.3. *Effect of persistence length on K_{eff} of nanocomposites*

To compare with our previous work for the case of straight CNTs [107], we performed isoflux simulations on a CNT-polystyrene system with various persistence lengths of CNTs at low CNT loading. We controlled the configurations of CNTs by changing the critical angles ($\varphi_{critical}$ and $\phi_{critical}$) between two segments from 90° to 5.4^o (Figure 6.3.4). As tabulated in Table 6.3.2, the CNT can be considered under significant bending ($L \gg L_p$) or semi-flexible ($L \approx L_p$). The $TBR_{CNT\text{-}PS}$ at 25^oC is equal to 2.2×10^{-8} $W^{-1}m^2K$, which has been calculated in ref. [107] and was used as input for this work. It is reasonable to ignore $TBR_{CNT\text{-}CNT}$ in this work since the vol.% of CNTs was low.

<center>a)   b)</center>
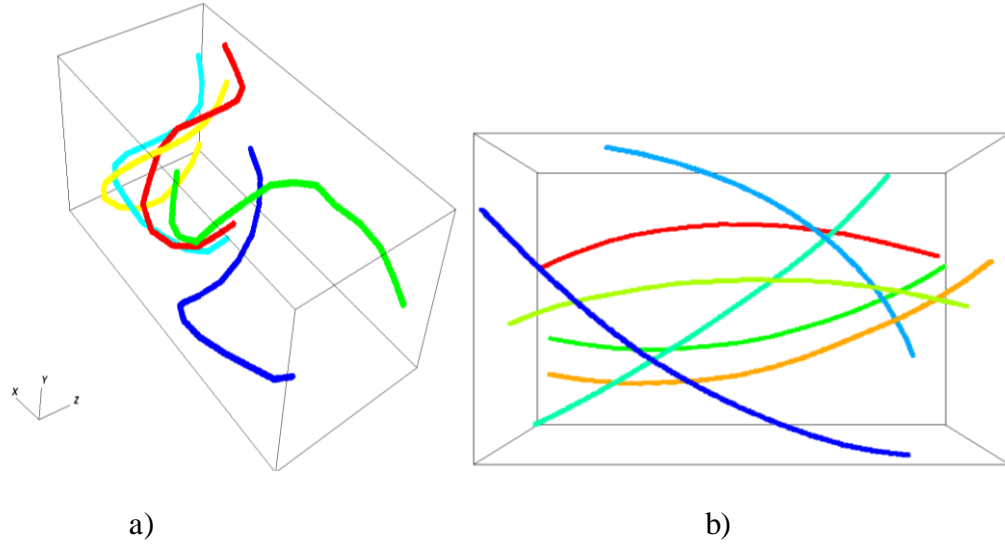
Figure 6.3.4. Worm-like CNTs , with 15 segments/CNT, generated inside a computational box of 450x300x300 mesh points are used in isoflux simulations to calculate effective thermal conductivity. The contour length of each CNT is fixed at 450nm and the persistence length is varied in each case: a) L_p =68.4nm , b) L_p = 527.4nm.

Table 6.3.2. Values of persistence length, L_p, and end-to-end length, L_e, of the worm-like CNTs were controlled by changing the critical angles between two segments. The contour length was fixed at 450nm for all cases.

$\theta_{critical} = \varphi_{critical}$	90.0^o	43.2^o	21.6^o	10.8^o	5.4^o
Average L_p (nm)	33.6	68.4	132.6	280.3	527.4
Average L_e (nm)	126.2	174.5	292.7	353.5	431.2
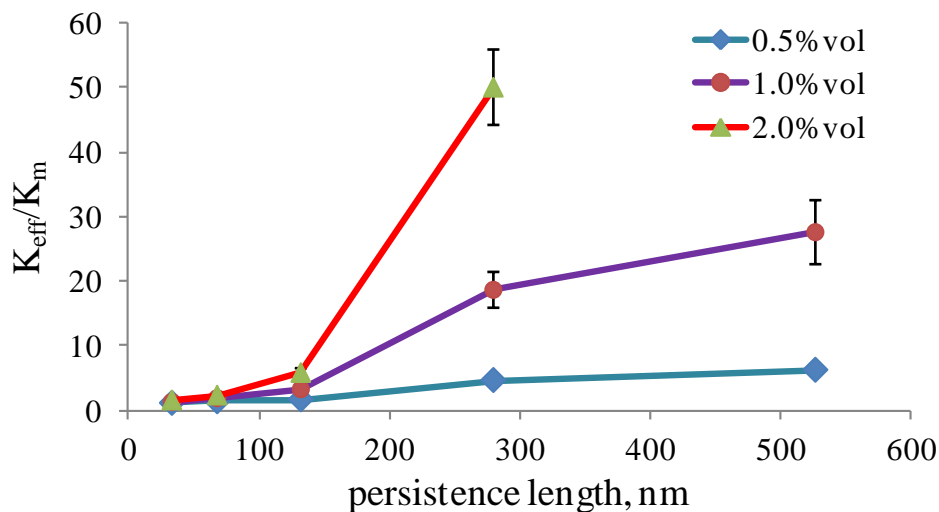
Figure 6.3.5. Effect of persistence length on ratio of thermal conductivity of composites over polymer (K_{eff}/K_m) for CNT-polystyrene system. The error bar is standard deviation calculated from 6 different runs (6 different CNT configurations). Other parameters of CNTs are tabulated in Table 6.3.2.

As we can see in Figure 6.3.5, since the persistence length of CNTs increases from 33.6nm to 280.3nm, K_{eff}/K_m of the system increases from 1.6 up to 50.0 for the same CNT vol.% . Also, by comparing K_{eff} calculated under the same conditions in our previous work for the case of straight CNTs [107], we found that worm-like CNTs with L= 450nm and L_p in the range from 33.6 to 68.4nm exhibit K_{eff} almost equal to that of straight CNTs with a length of L= 64nm.

6.3.4. *Contour length versus persistence length*

Up to this point, we found evidence that short CNTs with high persistence length can potentially have better contribution toward thermal transfer in nanocomposites compared to long CNTs under significant bending ($L \gg L_p$). This hypothesis was tested by conducting isoflux simulations at 1.0vol% of CNT, in which both the L and L_p of CNTs were varied over a wide range. For example, we increased L from 150nm to 750nm while decreasing L_p from 812nm to 30nm. As tabulated in Table

6.3.3, although L was decreased from 750nm to 450nm, K_{eff}/K_m increased from 1.79 to 6.94. That improvement is explained because of the increase in L_p. However, when the CNT is too short ($L < 450$nm), the K_{eff}/K_m ratio decreased from 6.94 to 1.14 regardless of the higher values of L_p in these cases.

Table 6.3.3. Relative thermal conductivity (K_{eff}/K_m) of nanocomposites at different values of contour length (L) and persistence length (L_p). The variance of K_{eff}/K_m was calculated based on 5 different runs for each case (different CNT configurations). The vol% of CNTs is equal to 1% for all cases. Higher end-to-end length (L_e) of CNTs resulted in better heat transfer.

Average L_e (nm)	155	218	321	289	149
Average L_p (nm)	30	55	179	398	812
L (nm)	750	600	450	300	150
K_{eff}/K_m	1.79	2.74	6.94	2.96	1.14
Var(K_{eff}/K_m)	0.42	0.39	1.09	0.41	0.03

Values of end-to-end length of CNTs, L_e, in each case were also calculated for comparison. Note that L_e is a length parameter which is the result of the deviation from the contour length due to bending of the CNT. In other words, L_e accounts for both L and L_p in describing what is the realistic length of CNTs under experimental conditions. That explains why the tendencies of L_e and the K_{eff}/K_m ratio are the same.

6.3.5. Validation with experiments

Generally, those parameters affecting K_{eff} of nanocomposites include Kapitza resistance (TBR$_{CNT\text{-}polymer}$, TBR$_{CNT\text{-}CNT}$), configuration (R, L_p, L), orientation and vol.% of CNTs. Experimental results of Guo *et al.*[144] for MWNT/epoxy will be used as

validation for our simulations. As discussed in Chapter 3, it is reasonable to ignore TBR$_{CNT-CNT}$ at low vol.% and the CNTs are randomly oriented according to experimental conditions. A value of TBR$_{CNT-epoxy}$ = 4.01x10^{-8} W^{-1}m^{2}K, as found in the literature[64], was used as input to our simulations. Average value of L_p (calculated from 50 configurations of MWNT) with and without the coating were calculated to be 294nm and 272nm from the TEM images, respectively. That means the thin layer of coating, where the silica has been non-covalently coated on MWNT [144], did not alter the configuration of the nanotubes significantly. By keeping R, L_p and vol.% of CNTs to be the same as in the experiments, value of K_{eff}/K_m obtained from the simulations can be compared with experimental data. As we can see from Table 6.3.4, our simulations have successfully replicated the experimental results.

Table 6.3.4. Ratio of effective thermal conductivity of pristine MWNT/epoxy nanocomposites over that of epoxy (K_{eff}/K_m) from experiments (Guo *et al.*[144]) and from simulations. The standard deviation (stdev) was calculated based on 5 different runs for each case.

wt.% MWNT	vol.% MWNT	K_{eff}/K_m exp.	K_{eff}/K_m sim.	stdev
0.5	0.35	1.27	1.23	0.08
1.0	0.7	1.61	1.68	0.46

6.3.6. *How to improve K$_{eff}$ in nanocomposites*

The main purpose of our simulations is not only limited to replicate the experimental data but also to quantitatively provide suggestions to improve K_{eff}. Many works have been done to suppress TBR at the interface of nanoinclusions and polymer matrix by functionalization.[84, 85, 110, 123] By comparing K_{eff}/K_m ratio from experiments [144] with our simulations under similar conditions, we proved that the

silica coating can suppress TBR by 40% (Figure 6.3.6). According to our work, if there is any surface modification method that can reduce TBR by 82%, K_{eff}/K_m ratio can reach up to 2.2 compared to the value of 1.6 for the case of pristine MWNT/epoxy.
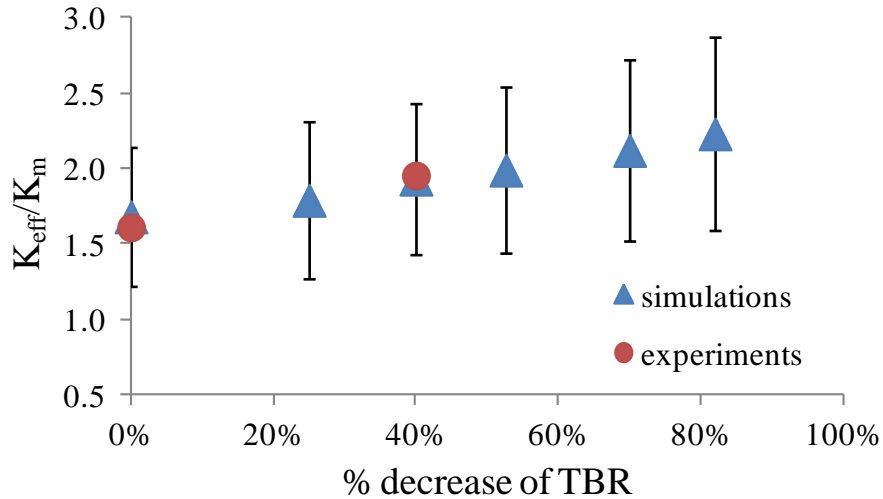
Figure 6.3.6. Ratio of effective thermal conductivity of 1wt.% MWNT/epoxy nanocomposites over that of pure polymer (K_{eff}/K_m) from experiments (red circles, Guo *et al.*[144]) and from simulations (blue diamond) as a function of thermal boundary resistance (TBR). The error bar was calculated based on 5 different runs for each case.

No prior work, by neither simulations nor experimental approach, has answered whether L_p of CNTs possesses a crucial effect on K_{eff} like TBR. As seen in Figure 6.3.7, the value of K_{eff}/K_m varies significantly with L_p of the nanotube. When increasing L_p by five times (from 270nm to 1428nm), the value of K_{eff}/K_m increases from 1.6 to 2.0. This enhancement is comparable to the value of $K_{eff}/K_m = 2.2$ that is obtained by decreasing the TBR by five times (82% of reduction as seen in Figure 6.3.6). We report here that L_p of the nanotube is as important as TBR toward heat transfer in nanocomposites.
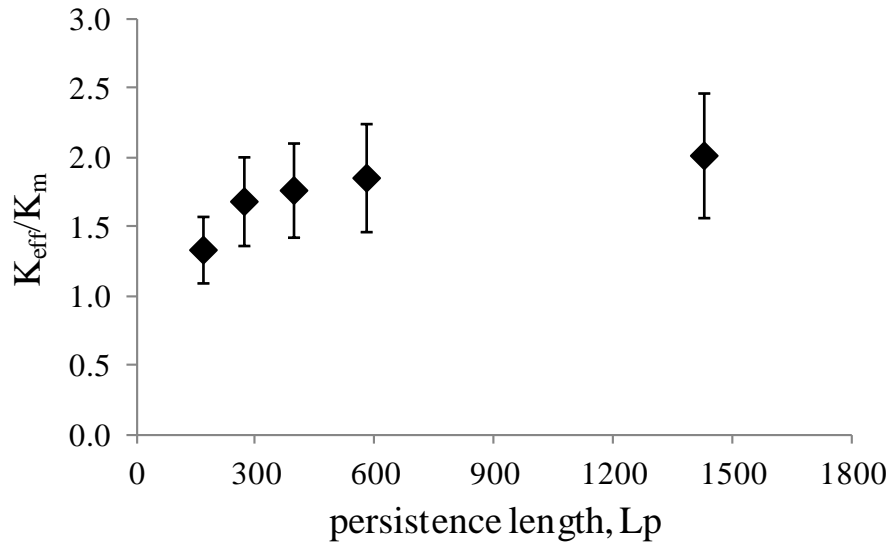
Figure 6.3.7. Effect of persistence length (L_p) on K_{eff}/K_m of 1wt.% pristine MWNT/epoxy. The error bar was calculated based on 5 different runs for each case.

6.4. Summary

We reported here a novel algorithm for generating worm-like CNTs in 3D with a realistic configuration. Our results suggest that shorter CNTs with high persistence length have stronger contribution toward heat transfer in nanocomposites compared to the case of longer CNTs under significant bending. We found that end-to-end length of CNTs was the most accurate parameter used to interpret the contribution of CNT length to the heat transfer in nanocomposites. This approach was validated with experiments for MWNT/epoxy systems. For the first time, we reported that L_p of the nanotube is as important as TBR toward heat transfer in nanocomposites.

Future Work

This work has provided an understanding of the Kapitza resistance between concentric nanotubes belonging to a DWNT, and between the outer nanotube and the amorphous silica coating. Nevertheless, there are still unanswered questions that require further work in this topic, such as:

- It is still unknown whether the Kapitza resistance is different along the axial direction of the nanotube. When a nanotube is long enough, the portion at the edge of the tube can be bended/moved quite easier than that at the middle of the tube. We believe the answer to this question can help to control the rate of heat transfer along the nanotube to the surrounding environment.

- Unlike the case of free standing DWNT, the presence of the silica coating has suppressed relative rotation between two concentric nanotubes. There should be another mechanism, in addition to the coupling strength between the vibrations of the carbon atoms, that helps to explain the dependence of Kapitza resistance on the chirality of CNTs.

The off-lattice Monte Carlo simulations developed in this work have provided a very accurate tool to predict K_{eff} in nanocomposites. This approach can also be used to investigate heat transfer in analogous systems such as carbon nanotube fibers and hierarchical carbon nanostructures. Again, a coherent use of both molecular dynamics and Monte Carlo simulations is a powerful key to unlock unanswered questions in this field.

References

[1]   W. E. Jones, J. Chiguma, E. Johnson, A. Pachamuthu, and D. Santos, Materials 3 (2010) 1478.
[2]   A. A. Balandin, IEEE Spectrum (2009) 29.
[3]   A. A. Balandin, Nature Materials 10 (2011) 569.
[4]   J. Hone, in Carbon Nanotubes, Vol. 80 (M. Dresselhaus, G. Dresselhaus, and P. Avouris, eds.), Springer Berlin / Heidelberg, 2001, p. 273.
[5]   H. O. Pierson, Handbook of Carbon, Graphite, Diamonds and Fullerenes: Processing, Properties and Applications, William Andrew, 1995.
[6]   E. T. Swartz and R. O. Pohl, Reviews of Modern Physics 61 (1989) 605.
[7]   J. M. Ziman, Electrons and Phonons: The Theory of Transport Phenomena in Solids, Oxford University Press, 2001.
[8]   R. B. Bird, W. S. Stewart, and E. N. Lightfoot, Transport Phenomena, Wiley, 2002.
[9]   A. Ward, D. A. Broido, D. A. Stewart, and G. Deinzer, Physical Review B 80 (2009) 125203.
[10] C. Jianwei, Ç. Tahir, and A. G. William, III, Nanotechnology 11 (2000) 65.
[11] S. Ghosh, I. Calizo, D. Teweldebrhan, E. P. Pokatilov, D. L. Nika, A. A. Balandin, W. Bao, F. Miao, and C. N. Lau, Applied Physics Letters 92 (2008) 151911.
[12] E. Munoz, J. X. Lu, and B. I. Yakobson, Nano Letters 10 (2010) 1652.
[13] L. X. Benedict, S. G. Louie, and M. L. Cohen, Solid State Communications 100 (1996) 177.
[14] J. Shiomi and S. Maruyama, International Journal of Thermophysics 31 (2010) 1945.
[15] P. L. Kapitza, Journal of Physics (Moscow) 4 (1941) 181.
[16] I. M. Khalatnikov, JETP 22 (1952) 687.
[17] G. L. Pollack, Reviews of Modern Physics 41 (1969) 48.
[18] W. A. Little, Canadian Journal of Physics 37 (1959) 334.
[19] E. T. Swartz and R. O. Pohl, Applied Physics Letters 51 (1987) 2200.
[20] B. V. Budaev and D. B. Bogy, Annalen der Physik 523 (2011) 208.
[21] B. V. Budaev and D. B. Bogy, Physics Letters A 374 (2010) 4774.
[22] B. V. Budaev and D. B. Bogy, Siam Journal on Applied Mathematics 70 (2010) 1691.
[23] A. Alzina, E. Toussaint, A. Béakou, and B. Skoczen, Composite Structures 74 (2006) 175.
[24] G. Balasubramanian and I. K. Puri, Applied Physics Letters 99 (2011) 013116.
[25] S. Pettersson and G. D. Mahan, Physical Review B 42 (1990) 7386.
[26] E. S. Landry and A. J. H. McGaughey, Physical Review B 80 (2009) 165304.
[27] H. A. Patel, S. Garde, and P. Keblinski, Nano Letters 5 (2005) 2225.
[28] H.-K. Lyeo and D. G. Cahill, Physical Review B 73 (2006) 144301.
[29] R. M. Costescu, M. A. Wall, and D. G. Cahill, Physical Review B 67 (2003) 054302.

[30] J. C. Maxwell, Treatise on Electricity and Magnetism, Dover Publications, 1954.
[31] L. Rayleigh, Philosophical Magazine 34 (1892) 481.
[32] D. P. H. Hasselman and L. F. Johnson, Journal of Composite Materials 21 (1987) 508.
[33] C.-W. Nan, R. Birringer, D. R. Clarke, and H. Gleiter, Journal of Applied Physics 81 (1997) 6692.
[34] C. W. Nan, G. Liu, Y. Lin, and M. Li, Applied Physics Letters 85 (2004) 3549.
[35] S. Kumar, M. A. Alam, and J. Y. Murthy, Journal of Heat Transfer 129 (2007) 500.
[36] S. Kumar, M. A. Alam, and J. Y. Murthy, Applied Physics Letters 90 (2007) 104105
[37] L. C. Davis and B. E. Artz, Journal of Applied Physics 77 (1995) 4954.
[38] J. Shiomi and S. Maruyama, Physical Review B 73 (2006) 205420.
[39] Q. Zhang, S. Rastogi, D. Chen, D. Lippits, and P. J. Lemstra, Carbon 44 (2006) 778.
[40] J. K. W. Sandler, J. E. Kirk, I. A. Kinloch, M. S. P. Shaffer, and A. H. Windle, Polymer 44 (2003) 5893.
[41] J. E. Peters, D. V. Papavassiliou, and B. P. Grady, Macromolecules 41 (2008) 7274.
[42] J. M. Haile, Molecular Dynamics Simulation: Elementary Methods, Wiley-Interscience, 1992.
[43] http://www.lammps.sandia.gov.
[44] J. Tersoff, Physical Review B 37 (1988) 6991.
[45] D. W. Brenner, Physical Review B 42 (1990) 9458.
[46] W. D. Brenner, A. S. Olga, A. H. Judith, J. S. Steven, N. Boris, and B. S. Susan, Journal of Physics: Condensed Matter 14 (2002) 783.
[47] N. Boris, L. Ki-Ho, and B. S. Susan, Journal of Physics: Condensed Matter 16 (2004) 7261.
[48] S. Shenogin, A. Bodapati, L. Xue, R. Ozisik, and P. Keblinski, Appl. Phys. Lett. 85 (2004) 2229.
[49] D. Konatham and A. Striolo, Applied Physics Letters 95 (2009) 163105.
[50] D. Konatham and A. Striolo, Nano Letters 8 (2008) 4630.
[51] D. P. D. F.P. Incropera, T.L. Bergman and A.S. Lavine, Fundamentals of Heat and Mass Transfer, John Wiley & Sons, 2007.
[52] M. S. Peters, Timmerhaus, K.D., Plant Design and Economics for Chemical Engineers, McGraw-Hill, New York, 1991.
[53] S. Maruyama, Y. Igarashi, Y. Taniguchi, and J. Shiomi, Journal of Thermal Science and Technology 1 (2006) 138.
[54] M. Vuorio, Journal of Physics Part C Solid State Physics 5 (1972) 1216.
[55] S. Berber, Y. K. Kwon, and D. Tománek, Physical Review Letters 84 (2000) 4613.
[56] A. A. Balandin, S. Ghosh, W. Bao, I. Calizo, D. Teweldebrhan, F. Miao, and C. N. Lau, Nano Letters 8 (2008) 902.
[57] Z.-Y. Ong and E. Pop, Journal of Applied Physics 108 (2010) 103502.
[58] H. M. Duong, D. V. Papavassiliou, L. L. Lee, and K. J. Mullen, Applied Physics Letters 87 (2005) 013101.

[59] D. V. Papavassiliou, International Journal of Heat and Mass Transfer 45 (2002) 3571.

[60] B. M. Mitrovic, P. M. Le, and D. V. Papavassiliou, Chemical Engineering Science 59 (2004) 543.

[61] R. S. Voronov, S. B. VanGordon, V. I. Sikavitsas, and D. V. Papavassiliou, International Journal for Numerical Methods in Fluids 67 (2010) 501.

[62] M. M. Tomadakis and S. V. Sotirchos, The Journal of Chemical Physics 98 (1993) 616.

[63] A. Einstein, Annals of Physics 17 (1905) 891.

[64] H. M. Duong, D. V. Papavassiliou, K. J. Mullen, and S. Maruyama, Nanotechnology 19 (2008) 065702.

[65] N. Fakhri, F. C. MacKintosh, B. Lounis, L. Cognet, and M. Pasquali, Science 330 (2010) 1804.

[66] H. S. Lee and C. H. Yun, Journal of Physical Chemistry C 112 (2008) 10653.

[67] A. N. Volkov and L. V. Zhigilei, ACS Nano 4 (2010) 6187.

[68] X. Duan, C. Tang, J. Zhang, W. Guo, and Z. Liu, Nano Letters 7 (2006) 143.

[69] G. Cao and X. Chen, Physical Review B 73 (2006) 155435.

[70] N. Fakhri, D. A. Tsyboulski, L. Cognet, R. B. Weisman, and M. Pasquali, Proceedings of the National Academy of Sciences 106 (2009) 14219.

[71] F. Gittes, B. Mickey, J. Nettleton, and J. Howard, The Journal of Cell Biology 120 (1993) 923.

[72] W. Zhou, M. F. Islam, H. Wang, D. L. Ho, A. G. Yodh, K. I. Winey, and J. E. Fischer, Chemical Physics Letters 384 (2004) 185.

[73] M. Sano, A. Kamino, J. Okamura, and S. Shinkai, Science 293 (2001) 1299.

[74] D. W. Schaefer, J. Zhao, J. M. Brown, D. P. Anderson, and D. W. Tomlin, Chemical Physics Letters 375 (2003) 369.

[75] H. S. Lee, C. H. Yun, H. M. Kim, and C. J. Lee, The Journal of Physical Chemistry C 111 (2007) 18882.

[76] D. V. Papavassiliou and T. J. Hanratty, International Journal of Heat and Mass Transfer 40 (1997) 1303.

[77] K. Bui, H. M. Duong, A. Striolo, and D. V. Papavassiliou, The Journal of Physical Chemistry C 115 (2011) 3872.

[78] M. B. Bryning, D. E. Milkie, J. M. Kikkawa, and A. G. Yodh, Applied Physics Letters 87 (2005) 161909.

[79] H. M. Duong, N. Yamamoto, D. V. Papavassilliou, S. Maruyama, and B. L. Wardle, Nanotechnology 20 (2009) 155702.

[80] H. M. Duong, N. Yamamoto, K. Bui, D. V. Papavassiliou, S. Maruyama, and B. L. Wardle, The Journal of Physical Chemistry C 114 (2010) 8851.

[81] H. M. Duong, D. V. Papavassiliou, K. J. Mullen, B. L. Wardle, and S. Maruyama, Journal of Physical Chemistry C 112 (2008) 19860.

[82] H. M. Duong, D. V. Papavassiliou, K. J. Mullen, B. L. Wardle, and S. Maruyama, International Journal of Heat and Mass Transfer 52 (2009) 5591.

[83] N. Shenogina, R. Godawat, P. Keblinski, and S. Garde, Physical Review Letters 102 (2009)

[84] T. C. Clancy, S. J. V. Frankland, J. A. Hinkley, and T. S. Gates, International Journal of Thermal Sciences 49 (2010) 1555.

[85]   C. Schroder, V. Vikhrenko, and D. Schwarzer, Journal of Physical Chemistry A 113 (2009) 14039.

[86]   D. Konatham and A. Striolo, Applied Physics Letters 95 (2009) 163105.

[87]http://www.idtechex.com/research/reports/carbon_nanotubes_and_graphene_for_el ectronics _applications_technologies_players_and_opportunities_000229.asp

[88]   S. Stankovich, D. A. Dikin, G. H. B. Dommett, K. M. Kohlhaas, E. J. Zimney, E. A. Stach, R. D. Piner, S. T. Nguyen, and R. S. Ruoff, Nature 442 (2006) 282.

[89]   H. Kim, A. A. Abdala, and C. W. Macosko, Macromolecules 43 (2010) 6515.

[90]   D. Y. Cai and M. Song, Journal of Materials Chemistry 20 (2010) 7906.

[91]   T. Enoki, Y. Kobayashi, and K.-I. Fukui, International Reviews in Physical Chemistry 26 (2007) 609.

[92]   D. A. Areshkin, D. Gunlycke, and C. T. White, Nano Letters 7 (2006) 204.

[93]   J. Hu, X. Ruan, Z. Jiang, and Y. P. Chen, AIP Conference Proceedings 1173 (2009) 135.

[94]   J. Hu, S. Schiffli, A. Vallabhaneni, X. Ruan, and Y. P. Chen, Applied Physics Letters 97 (2010) 133107.

[95]   S. T. Huxtable, D. G. Cahill, S. Shenogin, L. Xue, R. Ozisik, P. Barone, M. Usrey, M. S. Strano, G. Siddons, M. Shim, and P. Keblinski, Nature Materials 2 (2003) 731.

[96]   T. C. Clancy and T. S. Gates, Polymer 47 (2006) 5990.

[97]   A. K. Roy, B. L. Farmer, S. Sihn, V. Varshney, S. Patnaik, and S. Ganguli, Diamond Relat. Mater. 19 (2010) 268.

[98]   Y. Huang, J. Wu, and K. C. Hwang, Physical Review B 74 (2006) 245413.

[99]   J. Yu, R. K. Kalia, and P. Vashishta, The Journal of Chemical Physics 103 (1995) 6697.

[100]   C. Li and T.-W. Chou, Physical Review B 73 (2006) 245407.

[101]   E. H. Hwang and S. Das Sarma, Physical Review B 77 (2008) 115449.

[102]   H. Zhong and J. R. Lukes, Physical Review B 74 (2006) 125403.

[103]   E. J. Garcia, B. L. Wardle, and A. John Hart, Composites Part A: Applied Science and Manufacturing 39 (2008) 1065.

[104]   E. J. Garcia, B. L. Wardle, A. John Hart, and N. Yamamoto, Composites Science and Technology 68 (2008) 2034.

[105]   B. Tonpheng, J. Yu, and O. Andersson, Macromolecules 42 (2009) 9295.

[106]   M. Fang, K. Wang, H. Lu, Y. Yang, and S. Nutt, Journal of Materials Chemistry 20 (2010) 1982.

[107]   K. Bui, B. P. Grady, and D. V. Papavassiliou, Chemical Physics Letters 508 (2011) 248.

[108]   A. Mierczynska, J. Friedrich, H. Maneck, G. Boiteux, and J. Jeszka, Central European Journal of Chemistry 2 (2004) 363.

[109]   A. Peigney, C. Laurent, E. Flahaut, R. R. Bacsa, and A. Rousset, Carbon 39 (2001) 507.

[110]   V. Varshney, S. S. Patnaik, A. K. Roy, and B. L. Farmer, The Journal of Physical Chemistry C 114 (2010) 16223.

[111]   Y. Takagi, T. Hosokawa, K. Hoshikawa, H. Kobayashi, and Y. Hiki, Journal of the Physical Society of Japan 76 (2007) 024604.

[112] H. Park, C. B. Park, C. Tzoganakis, K. H. Tan, and P. Chen, Industrial & Engineering Chemistry Research 47 (2008) 4369.

[113] N. Tsutsumi, S. Kizu, W. Sakai, and T. Kiyotsukuri, Journal of Polymer Science Part B: Polymer Physics 35 (1997) 1869.

[114] M. B. Jakubinek, M. A. White, M. Mu, and K. I. Winey, Applied Physics Letters 96 (2010) 083105.

[115] K. Bui, H. Nguyen, C. Cousin, A. Striolo, and D. V. Papavassiliou, The Journal of Physical Chemistry C 116 (2012) 4449.

[116] S. Bandow, M. Takizawa, K. Hirahara, M. Yudasaka, and S. Iijima, Chemical Physics Letters 337 (2001) 48.

[117] R. Saito, R. Matsuo, T. Kimura, G. Dresselhaus, and M. S. Dresselhaus, Chemical Physics Letters 348 (2001) 187.

[118] Y. A. Kim, H. Muramatsu, T. Hayashi, M. Endo, M. Terrones, and M. S. Dresselhaus, Chemical Physics Letters 398 (2004) 87.

[119] K. Koziol, J. Vilatela, A. Moisala, M. Motta, P. Cunniff, M. Sennett, and A. Windle, Science 318 (2007) 1892.

[120] J. Cumings and A. Zettl, Science 289 (2000) 602.

[121] S. Shenogin, L. Xue, R. Ozisik, P. Keblinski, and D. G. Cahill, Journal of Applied Physics 95 (2004) 8136.

[122] Z. Han and A. Fina, Progress in Polymer Science 36 (2011) 914.

[123] D. Konatham and A. Striolo, Applied Physics Letters 95 (2009) 163105.

[124] S. Kumar and J. Y. Murthy, Journal of Applied Physics 106 (2009) 084302.

[125] J. Yang, S. Waltermire, Y. Chen, A. A. Zinn, T. T. Xu, and D. Li, Applied Physics Letters 96 (2010) 023109.

[126] J. L. Rivera, C. McCabe, and P. T. Cummings, Nano Letters 3 (2003) 1001.

[127] S. Zhang, W. K. Liu, and R. S. Ruoff, Nano Letters 4 (2004) 293.

[128] N. A. Roberts and D. G. Walker, International Journal of Thermal Sciences 50 (2011) 648.

[129] N. A. Roberts and D. G. Walker, Journal of Heat Transfer 133 (2011) 092401.

[130] G. Wu and B. Li, Physical Review B 76 (2007) 085424.

[131] C. W. Chang, D. Okawa, A. Majumdar, and A. Zettl, Science 314 (2006) 1121.

[132] N. Yang, G. Zhang, and B. Li, Applied Physics Letters 95 (2009) 033107.

[133] D. Konatham, K. N. D. Bui, D. V. Papavassiliou, and A. Striolo, Molecular Physics: An International Journal at the Interface Between Chemistry and Physics 109 (2011) 97.

[134] K. A. Filippov and A. A. Balandin, Mrs Internet Journal of Nitride Semiconductor Research 8 (2003) 1.

[135] V. O. Turin and A. A. Balandin, Electronics Letters 40 (2004) 81.

[136] L. Hu, T. Desai, and P. Keblinski, Physical Review B 83 (2011) 195423.

[137] M. J. Biercuk, M. C. Llaguno, M. Radosavljevic, J. K. Hyun, A. T. Johnson, and J. E. Fischer, Applied Physics Letters 80 (2002) 2767.

[138] C. Guthy, F. Du, S. Brand, K. I. Winey, and J. E. Fischer, Journal of Heat Transfer 129 (2007) 1096.

[139] X. He, F. Zhang, R. Wang, and W. Liu, Carbon 45 (2007) 2559.

[140] A. K. Roy, B. L. Farmer, S. Sihn, V. Varshney, S. Patnaik, and S. Ganguli, Diamond and Related Materials 19 (2010) 268.

[141] N. Shenogina, S. Shenogin, L. Xue, and P. Keblinski, Applied Physics Letters 87 (2005) 133106.

[142] D. Konatham, D. V. Papavassiliou, and A. Striolo, Chemical Physics Letters 527 (2012) 47.

[143] R. Duggal and M. Pasquali, Physical Review Letters 96 (2006) 246104.

[144] P. S. Jiaxi Guo, Junfeng Liang, Mrinal Saha, Brian P. Grady, Submitted manuscript (2012).

Appendix: Potential Parameters

Lennard Jones potential parameters

Atoms	ε/k_B (K)	σ (Å)	cut-off (Å)
C – C	28.02	3.400	13.800
C – O	39.94	3.001	7.503
C – Si	103.38	3.326	8.315

The Tersoff potential is described as:

$$E = \sum_i E_i = \frac{1}{2}\sum_{i \neq j} V_{ij};$$

$$V_{ij} = f_C(r_{ij})\left[f_R(r_{ij}) + b_{ij} f_A(r_{ij}) \right];$$

$$f_R(r_{ij}) = A_{ij}\exp(-\lambda_{ij}r_{ij}), f_A(r_{ij}) = -B_{ij}\exp(-\mu_{ij}r_{ij});$$

$$b_{ij} = \chi_{ij}(1 + \beta_i^{n_i}\zeta_{ij}^{n_i})^{-1/2n_i}$$

$$\zeta_{ij} = \sum_{k \neq i,j} f_C(r_{ik})\omega_{ik} g(\theta_{ijk})$$

$$g(\theta_{ijk}) = 1 + c_i^2/d_i^2 - c_i^2/[d_i^2 + (h_i - \cos\theta_{ijk})^2]$$

$$\lambda_{ij} = (\lambda_i + \lambda_j)/2, \mu_{ij} = (\mu_i + \mu_j)/2, A_{ij} = (A_iA_j)^{1/2}, B_{ij} = (B_iB_j)^{1/2}, R_{ij} = (R_iR_j)^{1/2}, S_{ij} = (S_iS_j)^{1/2}$$

Tersoff potential parameters for carbon[**]

A (eV)	1.3936×10^3
B (eV)	3.467×10^2
λ (Å^{-1})	3.4879
μ (Å^{-1})	2.2119
β	1.5724×10^{-7}
n	7.2751×10^{-1}
c	3.8049×10^4
d	4.384×10^0
h	-5.7058×10^{-1}
R (Å)	1.95
S (Å)	0.15

** Lammps http://lammps.sandia.gov/doc/pair_tersoff.html